Pages 75 to 137 (Chapter 4.1)

Effects of Oxide film, Fe-rich phase, Porosity and their Interactions on Tensile Properties of Cast Al-Si-Mg Alloys

Kittiphan Bangyikhan

A thesis submitted to the Faculty of Engineering of
The University of Birmingham
for the degree of
Doctor of Philosophy

School of Metallurgy and Materials
Faculty of Engineering
University of Birmingham
Birmingham B15 2TT
United Kingdom
June 2005

CHAPTER 4

EXPERIMENTAL RESULTS

This chapter presents the tensile properties of the test bar castings produced, together with examinations of the defects observed on their fracture surfaces and the microstructure obtained from metallographic sections from the running system and test bars. These results have been analyzed to reveal any interactions between the microstructural defects studied, namely, Fe-rich phase, oxide films, and porosity caused by hydrogen gas and shrinkage. It also presents the microstructure and the image analysis results obtained from the high purity aluminium and the high purity Al-Si alloy casting experiments, carried out in order to examine the effect of oxide films on the nucleation of gas porosity. Finally, the experimental results obtained from plate castings made to analyze the interactions between oxide films and porosity, particularly shrinkage porosity, in the cast Al-Si-Mg alloy are also shown.

4.1 Interactions between Fe-rich phase, hydrogen porosity and oxide films in cast Al-7Si-0.3Mg alloy

4.1.1 Tensile properties

Tables 4.1 and 4.2 show the ultimate tensile strength (UTS) and elongation values for each test bar obtained from the 8 combinations of defects in the casting. They also show the mean UTS, mean elongation and the standard deviation for each experiment. Tables show that there were only 26 to 29 results from each combination, although 30 test bars were made. This is due to the damage of test bars occurred during the machining.

Table 4.1 Ultimate Tensile Strength (UTS) values for 8 experimental combinations.

Test bar No.	Ultimate Tensile Strength (UTS) (MPa)							
	1	2	3	4	5	6	7	8
1	296.84	257.98	286.47	218.97	276.74	257.88	247.13	254.94
2	296.14	274.25	279.37	276.04	279.03	274.76	251.87	244.93
3	308.57	299.10	288.83	271.99	287.31	277.60	258.90	262.27
4	298.07	302.14	279.37	191.31	281.85	294.67	254.68	243.68
5	302.44	289.45	271.36	241.51	261.96	255.57	258.37	251.55
6	311.38	306.07	281.55	268.29	266.94	260.54	257.67	258.70
7	298.94	295.53	285.92	264.94	247.08	279.91	256.26	162.69
8	304.02	291.41	284.62	279.39	272.28	257.88	261.35	203.10
9	310.15	305.18	282.88	278.40	258.79	182.34	263.29	237.96
10	308.75	295.70	281.83	268.82	270.32	254.32	242.21	229.38
11	294.21	274.25	277.11	269.35	275.34	244.90	247.13	236.35
12	297.71	310.36	275.02	268.41	281.85	257.70	268.29	245.11
13	312.74	295.55	287.00	275.86	250.15	235.86	245.66	230.63
14	304.42	249.12	273.54	273.93	258.25	283.88	252.01	238.85
15	309.13	293.24	287.77	264.77	251.38	240.63	256.56	245.65
16	300.34	304.80	278.68	262.65	275.34	281.68	260.99	262.92
17	311.27	302.02	285.50	261.77	291.37	295.07	267.25	252.51
18	310.36	293.60	270.32	276.15	279.56	274.76	251.24	207.08
19	307.35	305.33	287.92	270.50	266.70	137.38	262.76	246.97
20	315.05	300.64	261.47	274.56	281.10	260.49	266.97	234.32
21	309.39	116.86	279.59	263.71	267.22	224.32	256.04	73.58
22	309.48	289.13	270.25	263.43	280.63	286.59	260.84	233.49
23	302.97	292.31	268.97	268.20	268.44	252.93	270.14	238.67
24	299.82	259.56	273.31	266.19	275.12	284.84	262.34	242.95
25	307.35	282.74	282.44	262.97	275.69	197.40	258.78	223.75
26	310.39	157.34	271.53	263.84	280.80	267.49	260.61	251.48
27	311.91	247.28	274.41	273.81		246.97	251.83	218.84
28	298.41	310.48	275.11			264.59		255.78
29						254.86		204.66
Mean UTS (MPa)	305.27	278.62	278.65	263.70	271.59	254.75	257.45	230.79
Standard deviation (MPa)	5.99	44.03	7.00	18.34	11.47	34.32	7.16	37.00

Combination

1	low Fe, low H_2, low oxide film	5	high Fe, low H_2, low oxide film
2	low Fe, low H_2, high oxide film	6	high Fe, low H_2, high oxide film
3	low Fe, high H_2, low oxide film	7	high Fe, high H_2, low oxide film
4	low Fe, high H_2, high oxide film	8	high Fe, high H_2, high oxide film

Table 4.2 Elongation values for 8 experimental combinations.

Test bar No.	Elongation (%)							
	1	2	3	4	5	6	7	8
1	3.81	0.66	2.37	0.54	1.06	0.96	1.22	1.69
2	3.67	0.84	2.75	2.01	2.05	1.00	1.80	0.58
3	4.11	2.01	2.23	2.47	1.53	1.16	1.61	1.43
4	5.54	4.20	2.11	0.42	1.76	1.86	1.38	0.52
5	3.43	1.89	2.19	0.58	0.76	0.64	1.46	1.16
6	5.54	3.35	2.23	1.92	1.34	0.64	1.52	1.00
7	4.88	2.30	2.43	1.71	0.90	1.20	1.32	0.18
8	3.67	2.25	2.27	2.07	1.22	1.18	1.70	0.34
9	4.84	5.24	2.02	2.39	0.74	0.38	1.12	0.82
10	4.62	2.59	2.18	2.26	0.94	0.62	0.80	0.56
11	5.20	1.33	1.82	1.73	1.32	0.78	0.99	0.60
12	5.72	4.42	2.03	2.50	1.68	0.58	1.99	1.14
13	4.01	1.95	2.27	1.82	0.66	0.58	0.82	0.48
14	4.80	0.56	2.35	2.43	0.76	1.38	1.63	1.81
15	3.63	3.39	2.23	1.80	1.02	0.46	1.20	0.86
16	3.19	2.67	2.19	1.92	1.22	1.43	1.20	1.24
17	4.82	4.19	2.87	1.40	1.68	1.63	1.43	0.70
18	5.21	2.93	2.41	1.76	0.86	0.74	1.69	0.34
19	5.16	3.61	2.79	1.25	1.18	1.31	1.55	0.76
20	4.38	4.80	1.06	0.84	1.31	1.16	1.34	0.52
21	4.96	0.14	2.81	2.11	0.97	0.38	1.30	0.08
22	4.26	1.38	2.68	1.76	1.49	1.18	1.36	0.58
23	6.26	1.85	2.15	1.93	1.00	0.76	1.38	0.72
24	5.01	1.04	2.17	2.96	0.98	2.93	1.63	1.20
25	3.21	1.16	2.51	2.09	1.18	0.33	1.38	0.56
26	5.02	0.31	2.91	2.25	1.43	1.41	1.87	1.22
27	3.12	0.60	2.64	2.47		0.82	1.38	0.60
28	4.64	5.06	2.24			0.76		1.47
29						1.02		0.41
Mean Elongation (%)	4.52	2.38	2.32	1.83	1.19	1.01	1.41	0.81
Standard deviation (%)	0.84	1.53	0.37	0.64	0.35	0.54	0.29	0.44

Combination

1 low Fe, low H_2, low oxide film
2 low Fe, low H_2, high oxide film
3 low Fe, high H_2, low oxide film
5 high Fe, low H_2, low oxide film
6 high Fe, low H_2, high oxide film
7 high Fe, high H_2, low oxide film

4 low Fe, high H_2, high oxide film 8 high Fe, high H_2, high oxide film

As might be expected the combination of low oxide film content, low hydrogen gas and low Fe-rich phase had the highest UTS and elongation, (with a mean UTS of 305 MPa and mean elongation of 4.5%), while the high oxide film, high hydrogen gas and high Fe-rich phase combination had the lowest UTS and elongation, (mean UTS of 231 MPa and mean elongation of 0.81%). The best and the worst casting conditions resulted in a difference in mean UTS of 75 MPa and in mean elongation of 3.7%.

The data also illustrated that increasing the amount of each microstructural defect directly affected the tensile properties by decreasing the UTS and elongation. For example, the increase in Fe content from 0.1 to 0.5 wt% decreased the mean UTS and elongation by 34 MPa and 3.3 % respectively in the low hydrogen and low oxide film castings. The increase in hydrogen gas from 0.1 to 0.45 ml/100g metal resulted in a reduction in the mean UTS and elongation of 27 MPa and 2.2 % respectively in the low Fe and low oxide film castings. The increase in oxide film content resulted in a reduction in the mean UTS and elongation of 27 MPa and 2.1 % respectively in low Fe and low hydrogen castings.

The standard deviation is a statistic that shows how tightly all the various examples are clustered around the mean in a set of data. The standard deviation values for the high oxide film castings in Tables 4.1 and 4.2 show that the increase in oxide film content resulted in an increase in the standard deviation, for example, in the low Fe and low hydrogen content castings, the standard deviation of the UTS and elongation data increased from 6 to 44 MPa and from 0.8 to 1.5 % respectively, when a high amount of oxide film was introduced into the castings. This means that the tensile properties of castings were narrowly distributed in the low oxide film content castings but were spread more widely in the high oxide film content castings.

4.1.2 Pareto diagram of tensile properties

Yates' algorithm is a simple technique for estimating the effects and determining the sums of squares in a 2^k factorial design [Montgomery 2001]. Tables 4.3 and 4.4 respectively demonstrate the relative effects on the tensile strength and elongation of the three microstructural defects, and their interrelationships obtained using Yates' algorithm. The sign obtained in the estimate of effect column showed how the defects influenced tensile properties, for example, a minus value meant that increasing the defect in the casting resulted in a reduction in tensile properties, a positive value indicated that the defect resulted in an increase in tensile properties.

Table 4.3 The effect of Fe-rich phase, hydrogen porosity, oxide film and their interactions on ultimate tensile strength (UTS) using Yate's algorithm.

	total	1	2	3	estimate of effect
(1)	305.27	576.86	1112.96	2140.82	535.21
A (effect of Fe-rich phase)	271.59	536.10	1027.86	-111.66	-27.92
B (effect of gas porosity)	278.65	533.37	-54.88	-79.64	-19.91
AB	257.45	494.49	-56.78	3.44	0.86
C (effect of oxide film)	278.62	-33.68	-40.76	-85.10	-21.27
AC	254.75	-21.20	-38.88	-1.90	-0.48
BC	263.70	-23.87	12.48	1.88	0.47
ABC	230.79	-32.91	-9.04	-21.52	-5.38

Table 4.4 The effect of Fe-rich phase, hydrogen porosity, oxide film and their interactions on elongation using Yate's algorithm.

	total	1	2	3	estimate of effect
(1)	4.52	5.72	9.45	15.48	3.87
A (effect of Fe-rich phase)	1.19	3.73	6.03	-6.62	-1.66
B (effect of gas porosity)	2.32	3.39	-4.24	-2.74	-0.69
AB	1.41	2.64	-2.39	2.78	0.69
C (effect of oxide film)	2.38	-3.33	-1.99	-3.41	-0.85
AC	1.01	-0.91	-0.75	1.85	0.46
BC	1.83	-1.37	2.42	1.24	0.31
ABC	0.81	-1.02	0.35	-2.07	-0.52

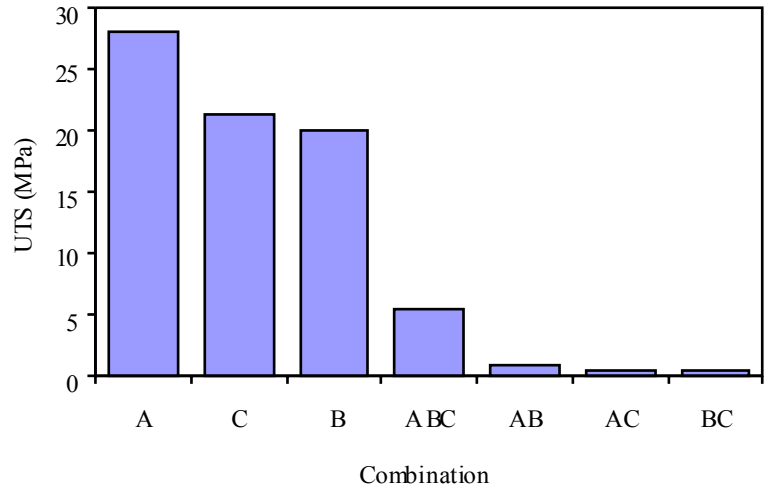

(a)

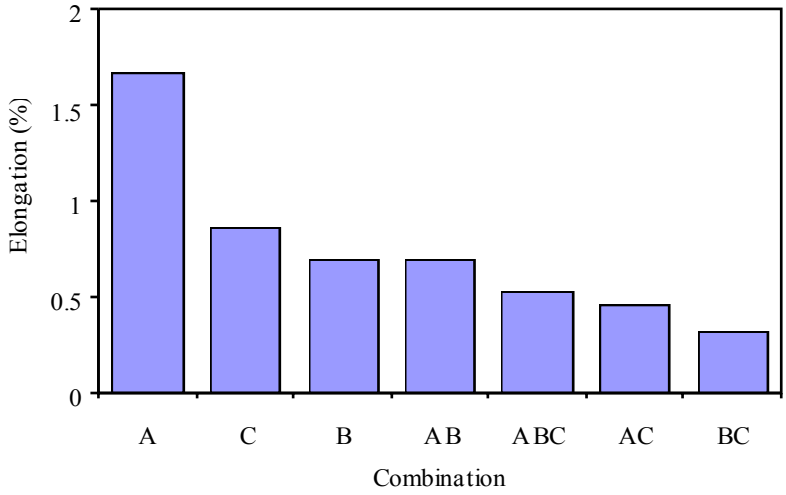

(b)

Figure 4.1 Pareto diagrams showing (a) the effects of the three defects and their interrelationships on the UTS and (b) on percent elongation of the castings. (A = Fe-rich phase, B = hydrogen porosity, C = oxide film defect)

Figures 4.1a and 4.1b show the Pareto diagrams obtained from the results in Tables 4.3 and 4.4 respectively. Each column in the Pareto diagrams shows the magnitude of the effect produced by the microstructural defects or any interactions between them. For example, column A and column B refer to the effect on the tensile properties of the presence of Fe-rich phase and hydrogen porosity respectively. Column ABC refers to the further effects that associated with an interaction between Fe-rich phase, hydrogen porosity and oxide film defects.

The diagrams show that the Fe-rich phases were the most detrimental to tensile strength and elongation (column A), compared to oxide films (column C) and hydrogen porosity (column B), which were in second and third places respectively (these rankings are true for the levels of defects introduced in this experiment). The effects of Fe-rich phases on ultimate tensile strength (UTS) and elongation were around 28 MPa and 1.7% respectively. This supports other results that the Fe-rich compounds, particularly platelet β-Al_5FeSi, are brittle, act as stress raisers and are therefore points of weakness in castings. The oxide films were the second most detrimental defect on tensile properties and had an effect on UTS of about 21 MPa and an effect on elongation of about 0.9%. The hydrogen porosity was the least detrimental in this experiment, producing an effect of about 20 MPa on UTS and 0.7% on elongation. Thus the Fe-rich phases, hydrogen porosity and oxide films had largely similar effects on the UTS values of the test bars whereas the Fe-rich phases strongly reduced the ductility of the alloy, compared to the other two defects.

The interactions between microstructural defects in the Pareto diagrams suggested an interaction between the Fe-rich phase, hydrogen porosity and oxide films (column ABC) that had the greatest effect on tensile properties. The diagrams show that, beside the effects individually produced by each defect, an interaction between these defects influenced the tensile properties by further decreasing the UTS by around 5 MPa and the elongation by around 0.5 %. This showed that the reduction of tensile properties in the high Fe-rich phase, high hydrogen porosity and high oxide film casting was caused by the effect of Fe-rich phases (28 MPa and 1.7%), the effect of hydrogen porosity (20 MPa and 0.7%), the effect of oxide film defects (21 MPa and 0.9%), and the effect an interaction between them (5 MPa and 0.5%), compared to the low Fe-rich phase, low hydrogen porosity and low oxide film casting. The Pareto diagram for elongation suggested some interaction between the Fe-rich phase and hydrogen porosity (column AB), the Fe-rich phase and oxide films (column AC), and the hydrogen porosity and oxide films (column BC). The elongation results seemed to be more sensitive and revealed interactions between defects more clearly than did the tensile strength results.

4.1.3 Examination of fracture surfaces

The fracture surfaces obtained from each experimental combination were observed by scanning electron microscopy (SEM). A number of cracked Fe-rich phases and Si particles were observed on the fracture surfaces of all test bars. Figures 4.2a and 4.2b show fracture surfaces of the low Fe, low hydrogen, and low oxide film castings and the EDX analysis results obtained from these particles has been shown in Figures 4.3a and 4.3b. These cracks suggested that the Fe-rich phase and Si particles had brittle characteristics. Figures 4.4a and 4.4b show fracture surfaces of the high Fe, low hydrogen and low oxide film casting and the high Fe, high hydrogen and low oxide film casting respectively. Figures 4.5a and 4.5b show associated EDX analysis results. As can be expected for the high Fe content castings (0.5 wt%), Fe-rich phase, particularly the β-Al5FeSi phase formed in the platelet morphology, was easily observed on the fracture surfaces. These Fe-rich phases were greater in size compared to those in the low Fe content castings. Again, Fe-rich phases observed on the fracture surfaces normally contained cracks. Therefore, Fe-rich phase was likely to be an initiator of fracture in the casting and resulted in a decrease in the strength and ductility of cast aluminium alloys.

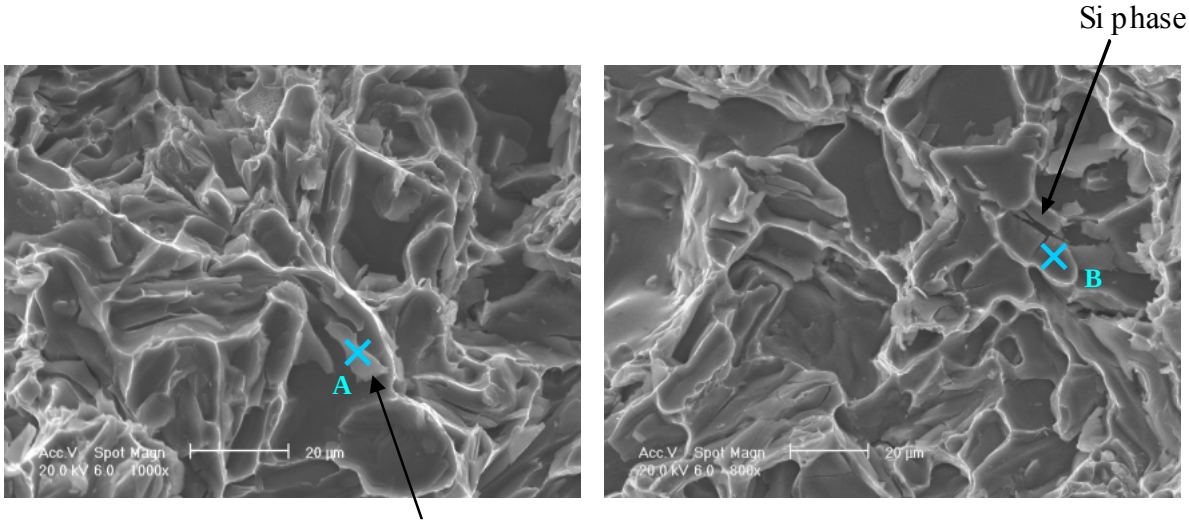

Figure 4.2 The scanning electron micrographs showing cracked particles on fracture surfaces of test bars obtained from the low Fe, low hydrogen and low oxide film casting.

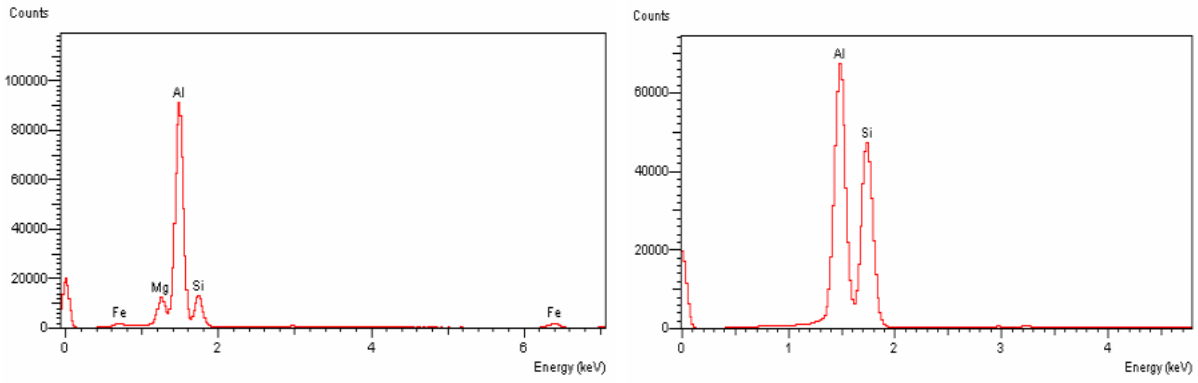

(a) (b)

Figure 4.3 The EDX analysis results obtained from points A and B in Figure 4.2a and 4.2b.

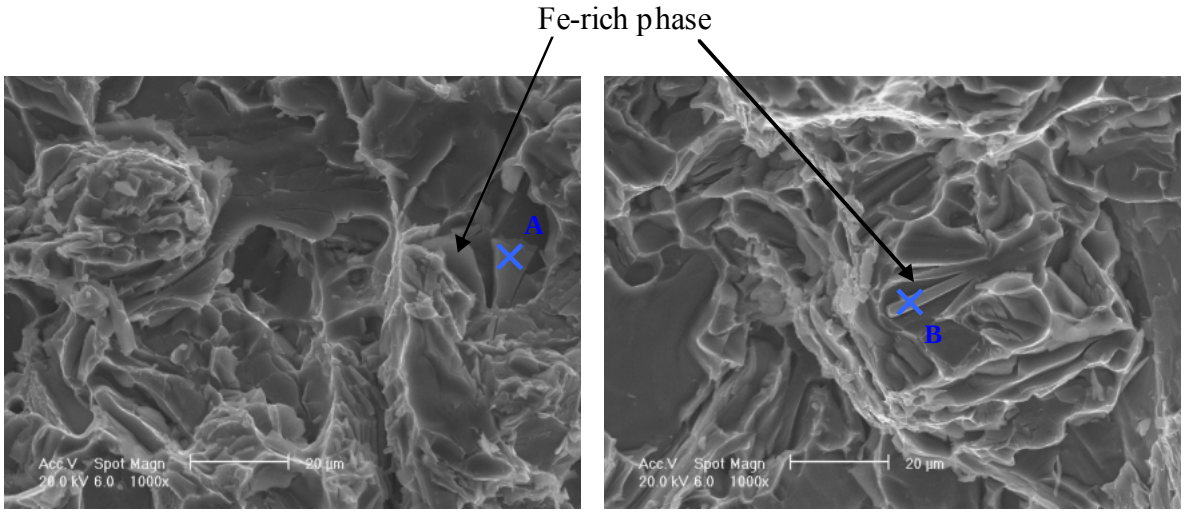

(a) (b)

Figure 4.4 The scanning electron micrographs showing cracked of Fe-rich phases on fracture surfaces of test bars obtained from a) the high Fe, low hydrogen and low oxide film casting and b) the high Fe, high hydrogen and low oxide film casting.

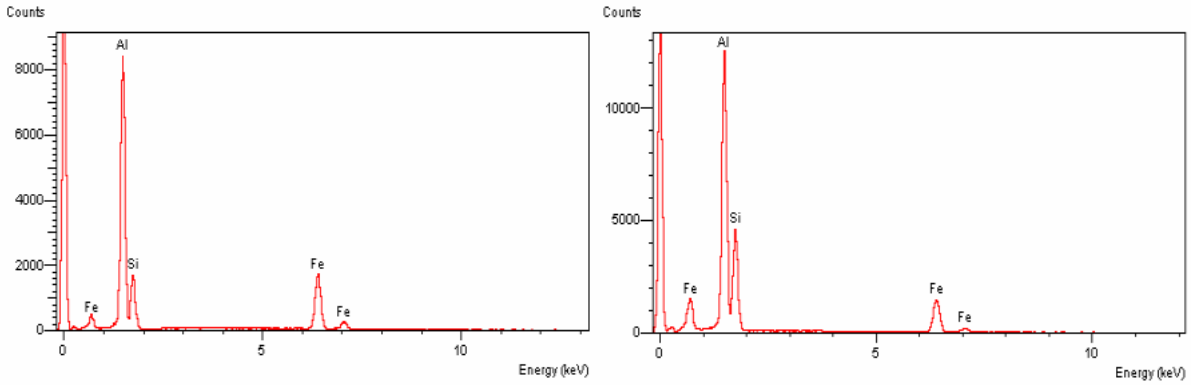

(a) (b)

Figure 4.5 The EDX analysis results obtained from points A and B in Figure 4.4a and 4.4b.

The fracture surfaces of the high oxide film castings were observed by digital camera and scanning electron microscopy. This showed that at least two test bars in every experimental combination contained a large oxide film defect, which was noticeable to the naked eye. Figure 4.6 shows fracture surfaces of test bar 26, obtained from the low Fe, low hydrogen and high oxide film combination. This test bar had a low UTS of 157 MPa and the observed fracture surfaces revealed that the great reduction in UTS was caused by the presence of a large double oxide film defect. The SEM images in Figures 4.7a to 4.7f show higher magnification images of the oxide films on both sides of the fracture surfaces and associated EDX analysis results have been shown in Figures 4.8a to 4.8f clearly showing the defect is an oxide film. As Figure 4.6 shows, the oxide film defect was symmetrical on both sides of the fracture surface, indicating the doubled nature of the oxide film defect.

Oxide films usually form on the surface of the melt when the molten aluminium alloy is exposed to an atmosphere of oxygen. The surface turbulence of the melt during transferring or filling process results in an entrainment of the oxide films into the melt. The non-wetted surfaces of the oxide films are separated by the residual entrained gas

and form a crack-like defect. The images showed that the oxide films on the two fracture surfaces had no bond between them and could be easily opened by the fracture. The EDX analysis showed that the oxide films observed were $MgO.Al_2O_3$ or spinel as would be expected to be formed in aluminium alloys containing magnesium [Campbell 2000]. Figures 4.9a and 4.9b show the wrinkled morphology of the oxide films and the EDX analysis of oxide film has been shown in Figure 4.9c.

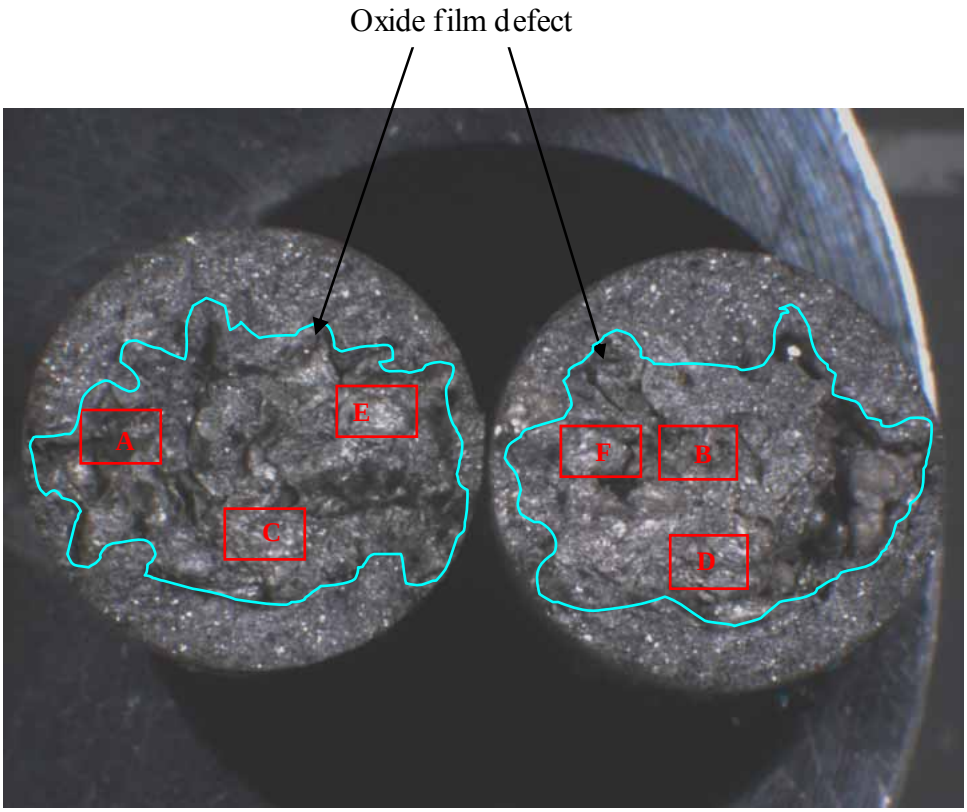

Figure 4.6 Photograph showing entrained oxide film defects on fracture surfaces of test bar 26 obtained from the low Fe, low hydrogen and high oxide film casting.

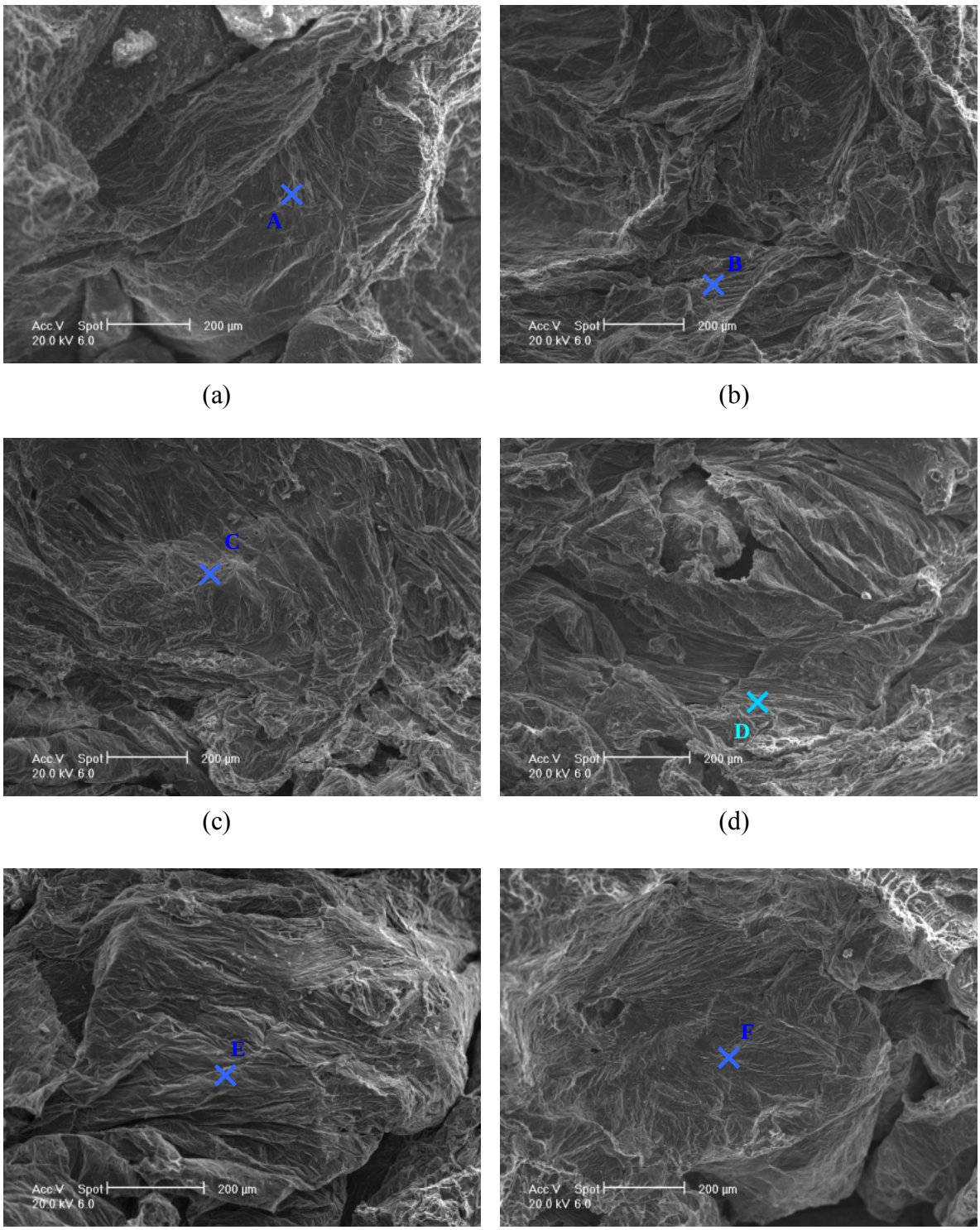

(a) (b)

(c) (d)

(e) (f)

Figure 4.7 The scanning electron micrographs showing the close-up images of oxide films on the fracture surfaces from areas A to F in Figure 4.6.

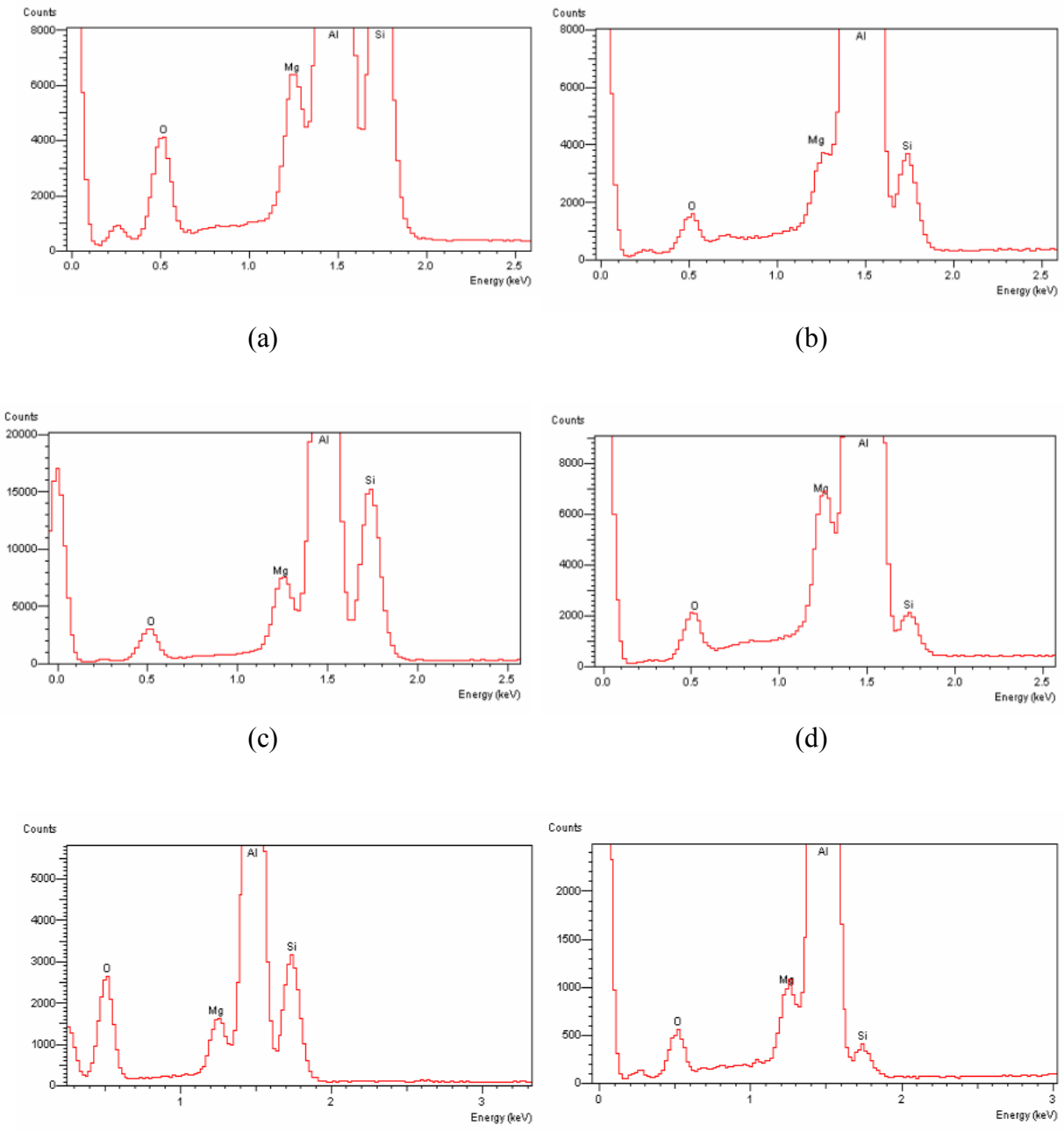

Figure 4.8 The EDX analysis results obtained from points A to F in Figures 4.7a to 4.7f.

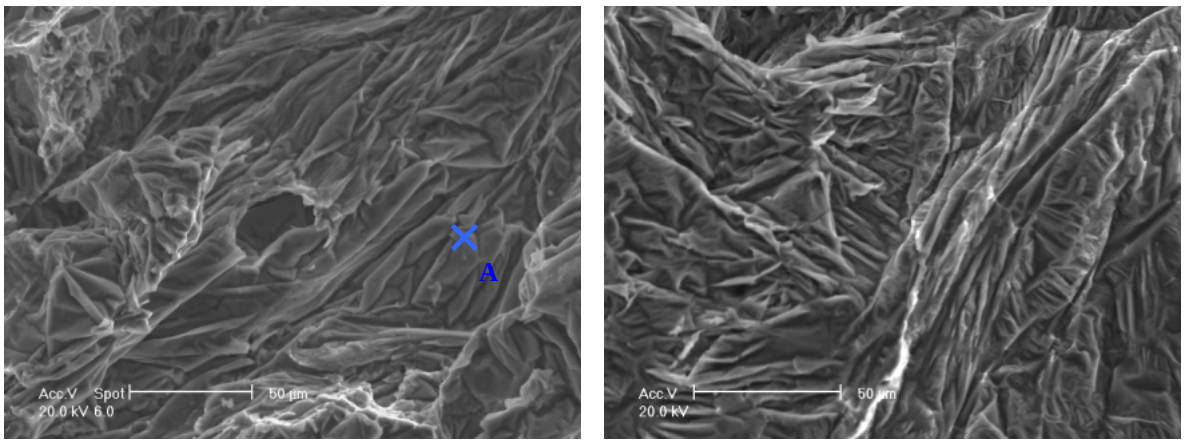

(a) (b)

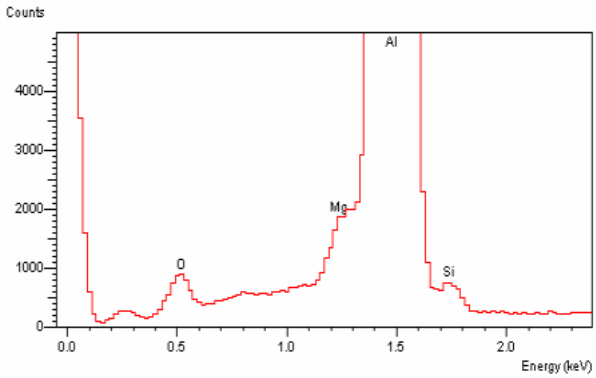

(c)

Figure 4.9 The scanning electron micrographs showing (a), (b) higher magnification of the oxide films defect in castings opened by the fracture, and (c) The EDX analysis result obtained from point A in Figure 4.9a.

The double oxide films can be an extremely serious defect in a casting since the folded oxide films can be all sizes and shapes. Figure 4.10 obtained from test bar 4 of the low Fe, high hydrogen and high oxide film castings shows large double oxide films on both sides of the fracture surfaces reaching from wall to wall of the test bar. The SEM images in Figures 4.11a to 4.11f and the EDX analysis in Figures 4.12a to 4.12f show large double oxide films that were opened during the tensile testing. This kind of defect resulted in a significant reduction in tensile properties, for example, test bar 4 had a UTS and elongation of only 191 MPa and 0.42%. The fracture surfaces of the other test bars

with low tensile properties were examined and all contained double oxide film defects. Figure 4.13 shows oxide films on both sides of the fracture surfaces obtained from test bar 25 of the high Fe, low hydrogen and high oxide film casting (UTS of 197 MPa and elongation of 0.33%). The SEM images of higher magnification have been shown in Figures 4.14a to 4.14d and the EDX analyses have been shown in Figures 4.15a to 4.15d. The fracture surfaces of test bar 7 obtained from the high Fe, high hydrogen and high oxide film casting (UTS of 163 MPa and elongation of 0.18%) have been shown in Figure 4.16. The SEM images of the oxide films on the fracture surfaces and their EDX analysis results have been shown in Figure 4.17a to 4.17d and Figures 4.18a to 4.18d respectively.

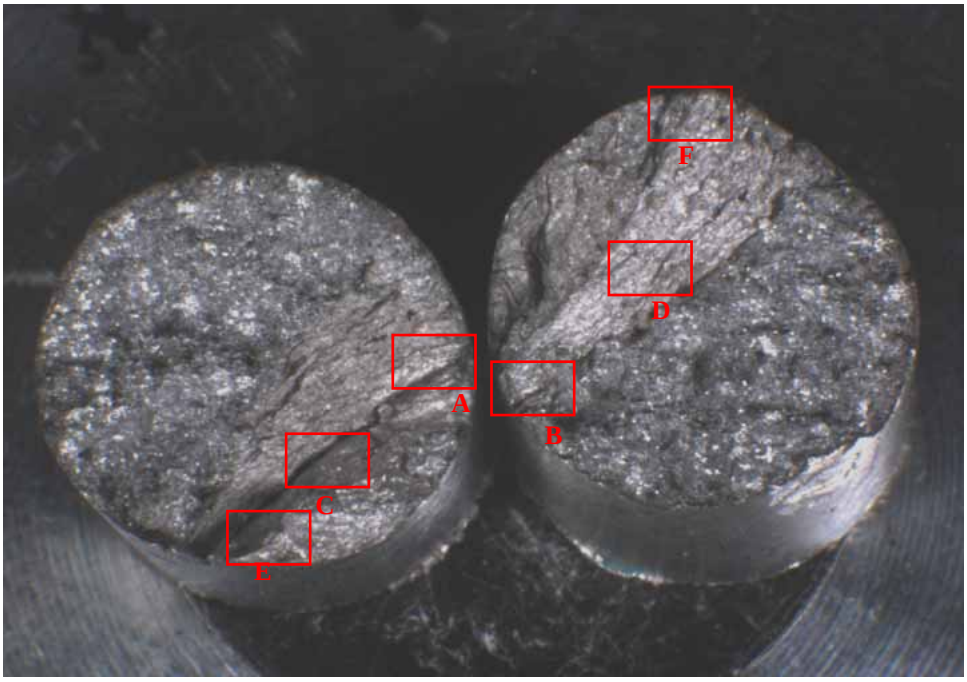

Figure 4.10 Photograph showing the fracture surfaces of test bar 4 obtained from the low Fe, high hydrogen and high oxide film casting.

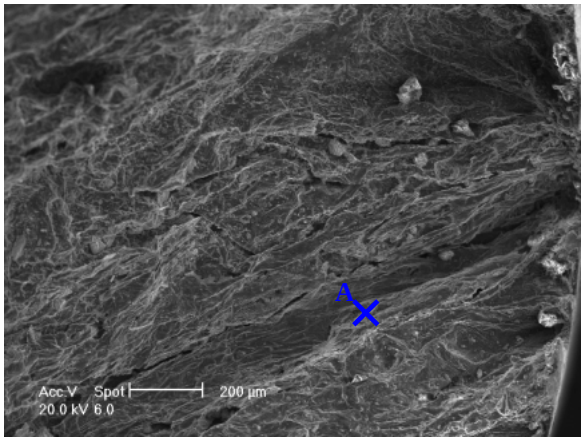

(a)

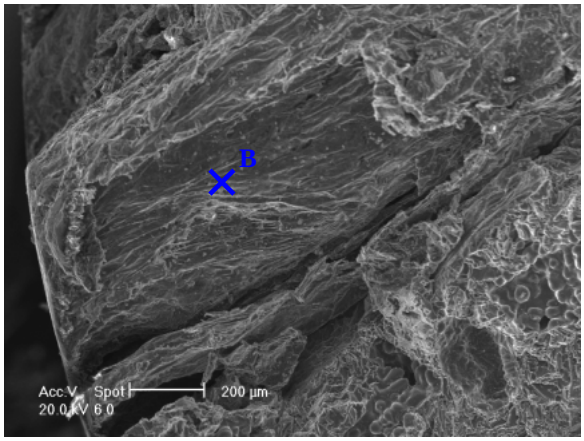

(b)

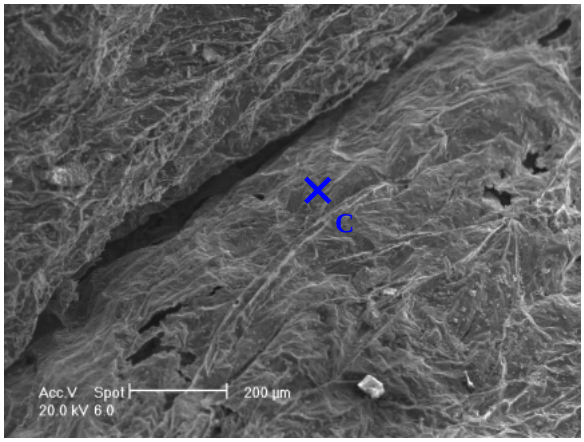

(b)

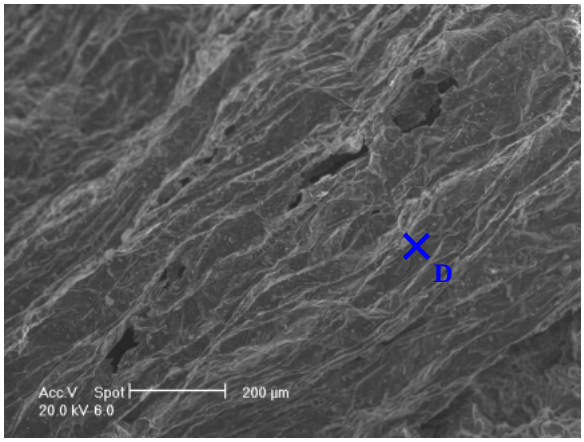

(d)

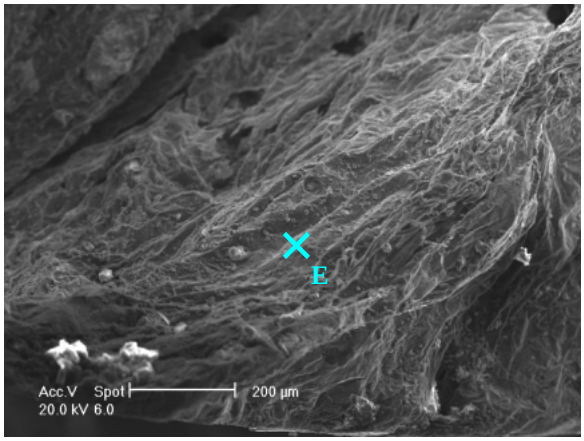

(e)

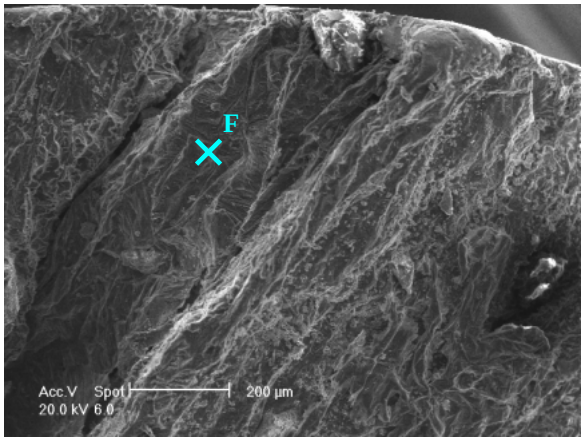

(f)

Figure 4.11 The scanning electron micrographs showing the close-up images of oxide films on the fracture surfaces from areas A to F in Figure 4.10.

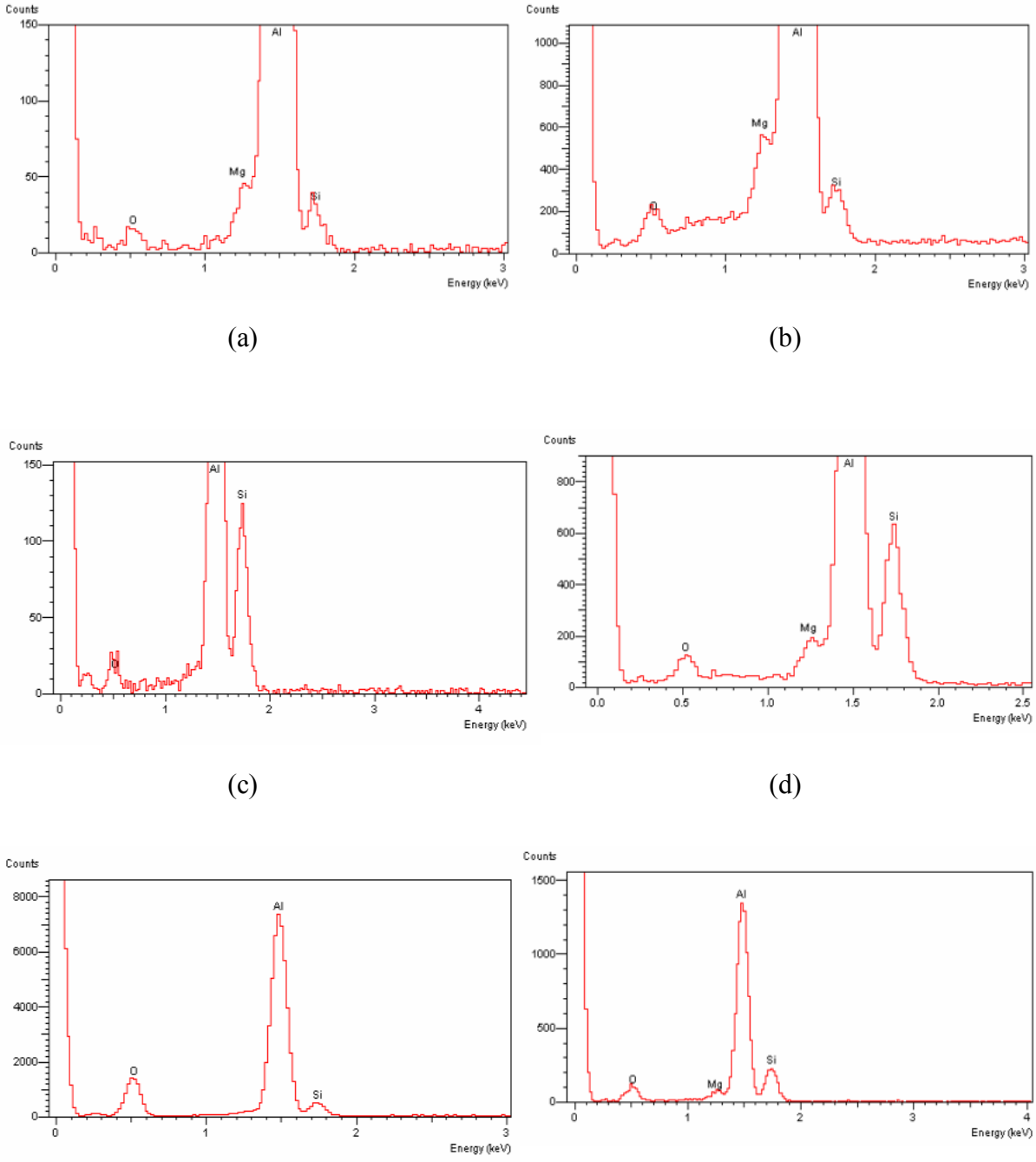

Figure 4.12 The EDX analysis results obtained from points A to F in Figures 4.11a to 4.11f.

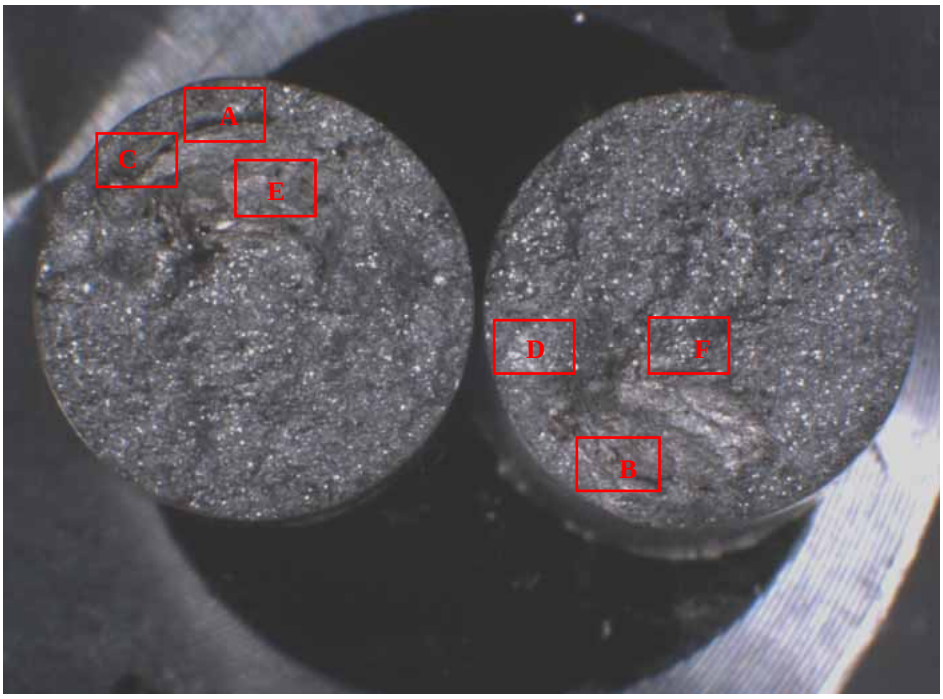

Figure 4.13 Photograph showing the fracture surfaces of test bar 25 obtained from the high Fe, low hydrogen and high oxide film casting.

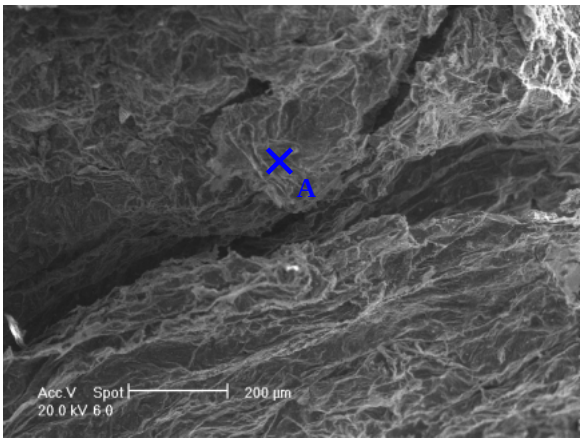

(a)

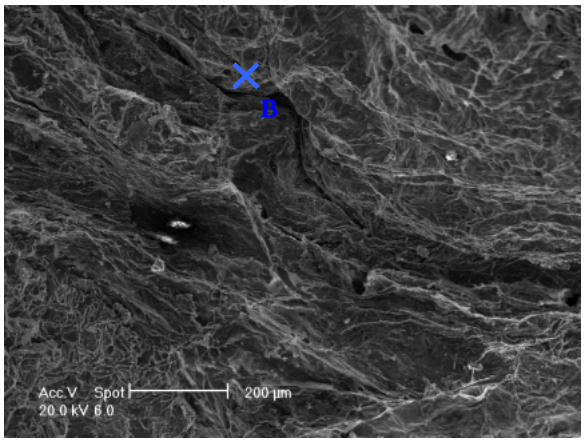

(b)

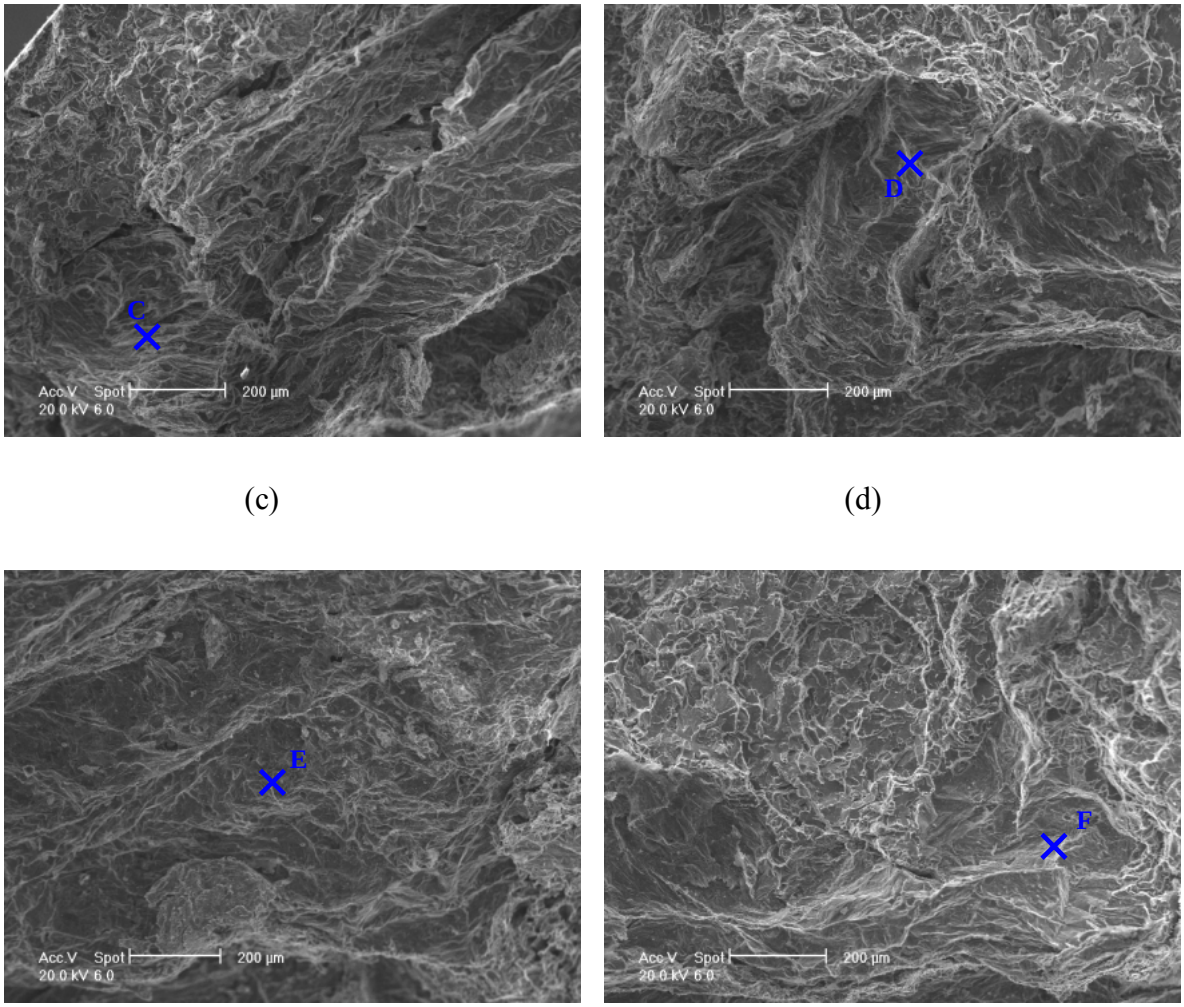

(c) (d)

(e) (f)

Figure 4.14 The scanning electron micrographs showing the close-up images of oxide films on the fracture surfaces from areas A to F in Figure 4.13.

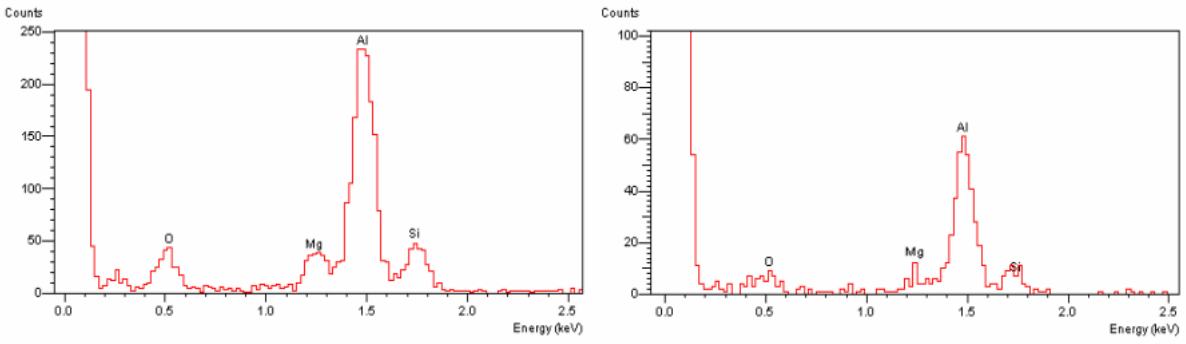

(a) (b)

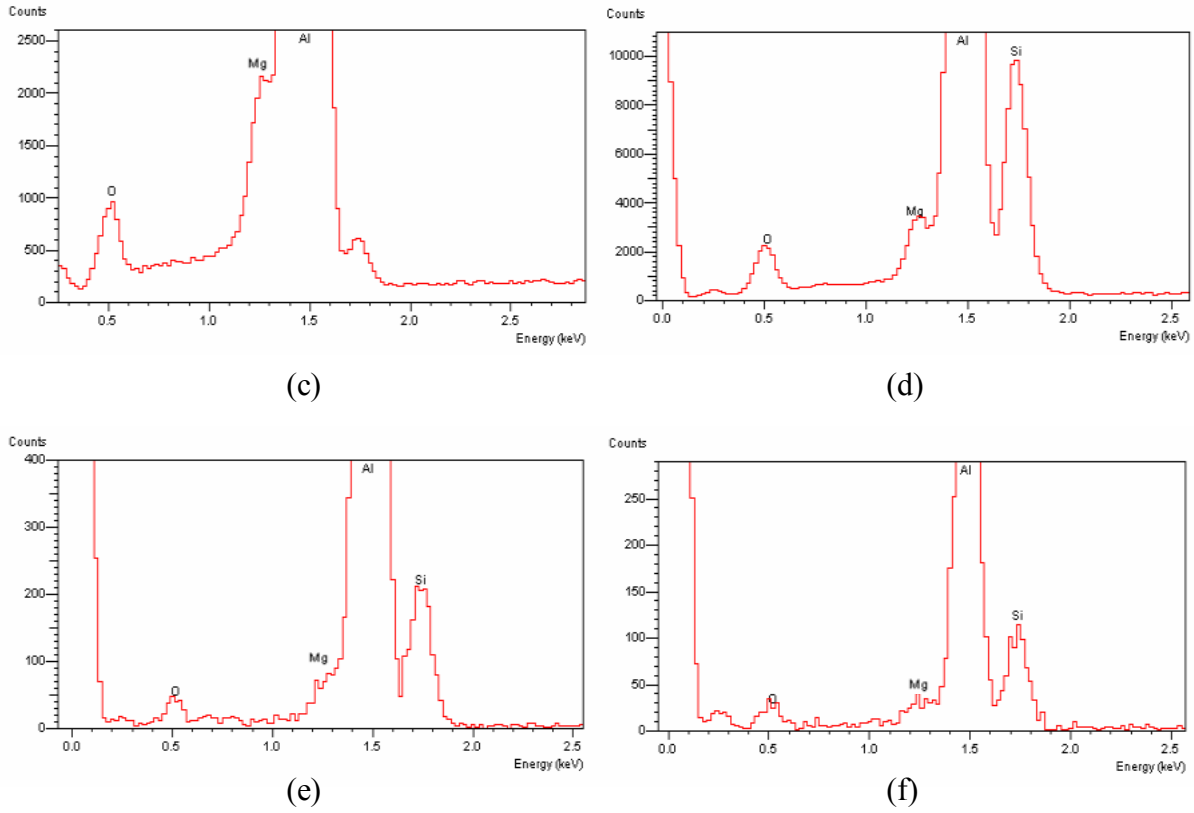

Figure 4.15 The EDX analysis results obtained from points A to F in Figure 4.14a to 4.14f.

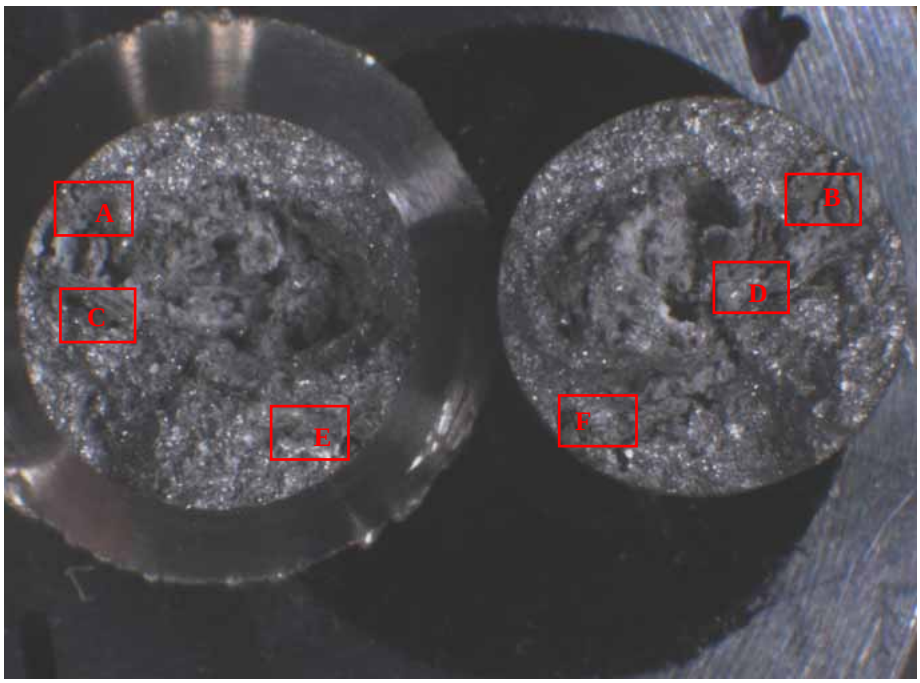

Figure 4.16 Photograph showing the fracture surfaces of test bar 7 obtained from the high Fe, high hydrogen and high oxide film casting.

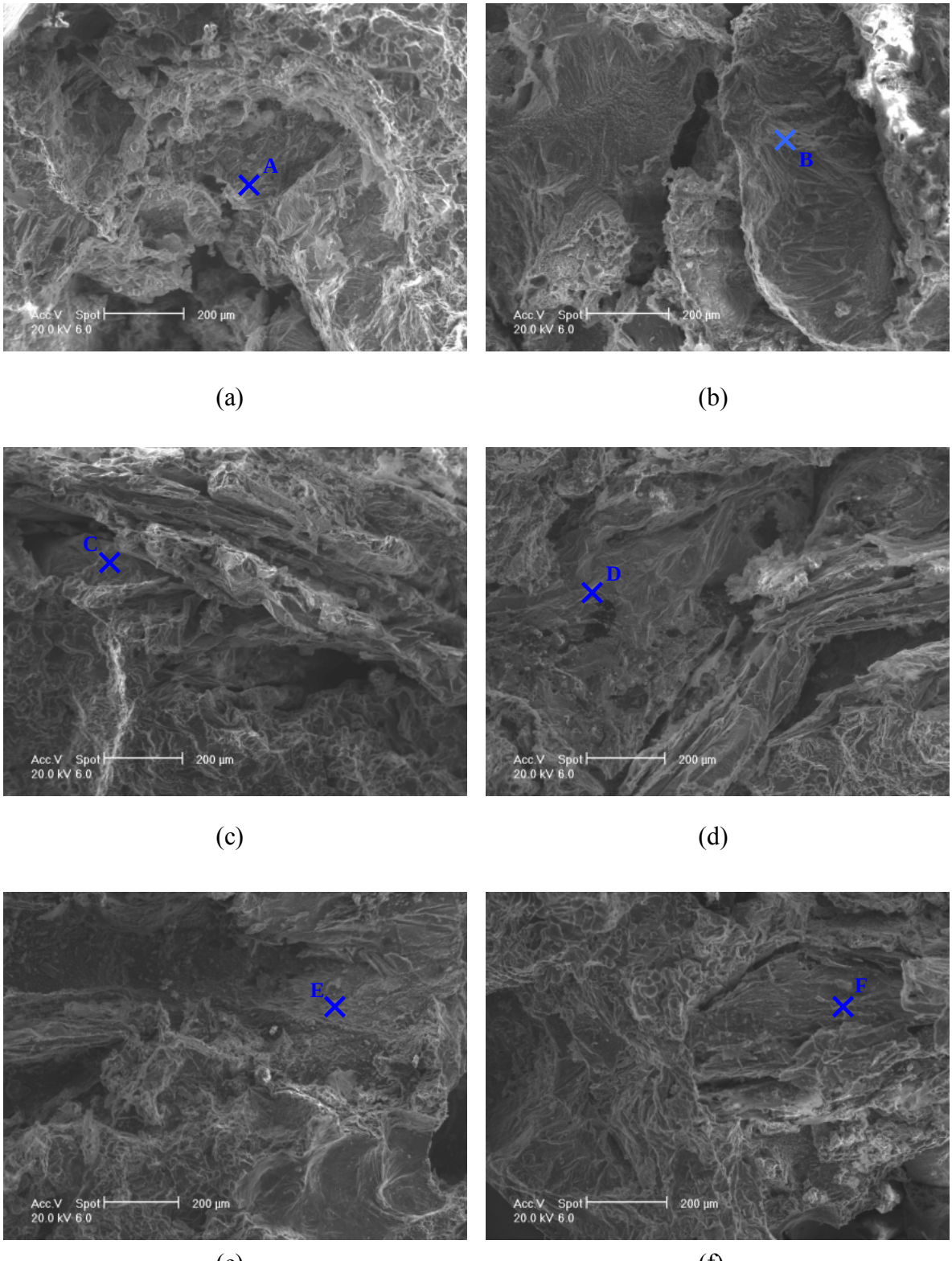

(a) (b)

(c) (d)

(e) (f)

Figure 4.17 The scanning electron micrographs showing the close-up images of oxide films on the fracture surfaces from areas A to F in Figure 4.16.

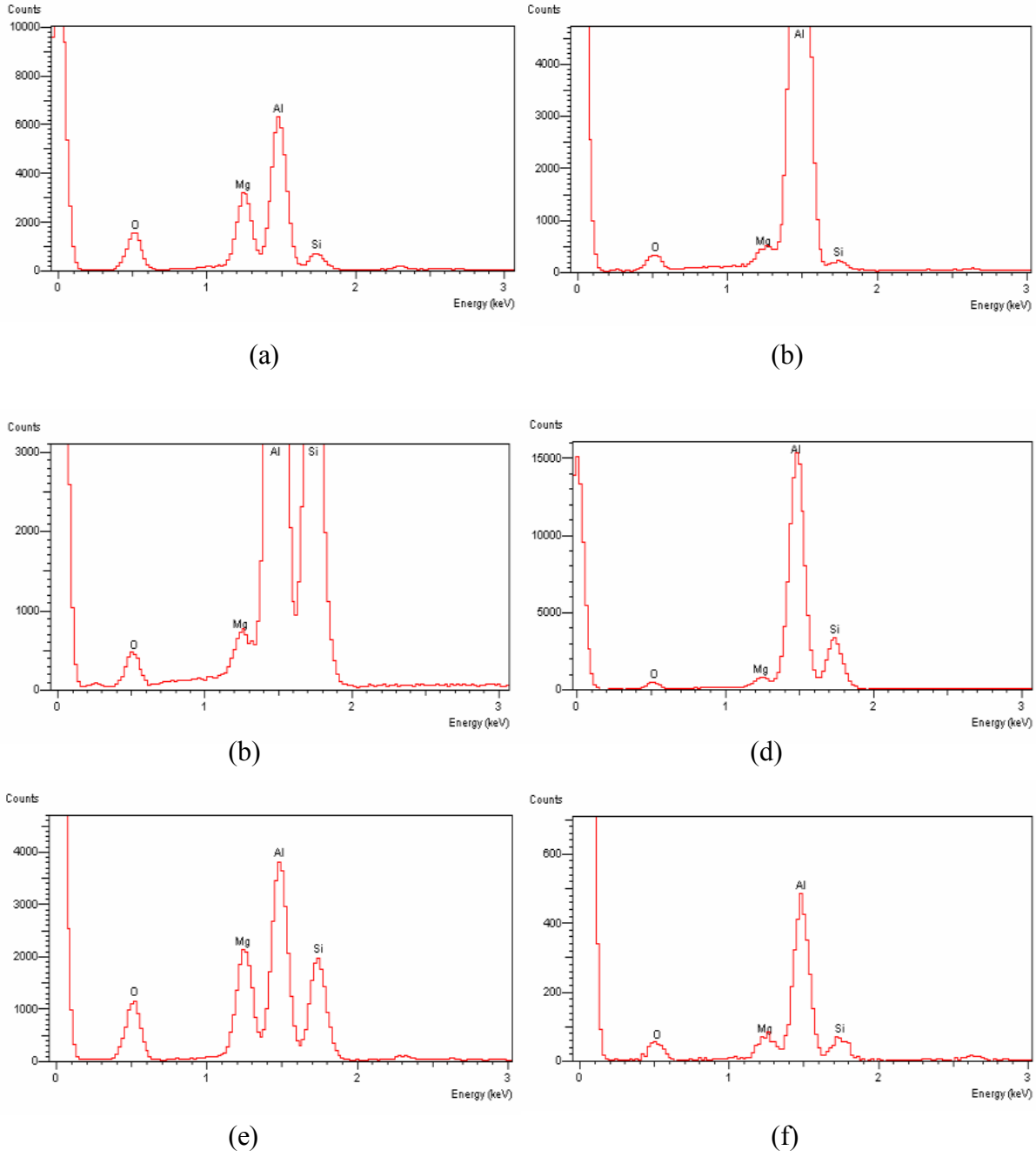

Figure 4.18 The EDX analysis results obtained from points A to F in Figures 4.17a to 4.17f.

In contrast, in the low oxide film castings, (the filtered castings), no extensive double oxide film defects were observed on the fracture surfaces by visual inspection. Figures 4.19a and 4.19b show the fracture surface of a test bar from a high hydrogen casting. It can be seen that the main defect observed was hydrogen gas porosity. This rounded porosity was likely to decrease tensile properties because it reduced the load bearing area.

On the other hand, although the filter was used in the low oxide films combination of the experimental castings in order to trap oxide film defects previously formed in the furnace and to decrease the velocity of liquid metal during mould filling, the presence of small double oxide films, of about 0.5 mm in length were observed. Figures 4.20a and 4.20b show both sides of the fracture surfaces obtained from a high Fe-rich phase, high hydrogen and low oxide film casting, (test bar 10). The EDX analysis results are shown in Figures 4.21a and 4.21b demonstrating that the defects are oxide films. Their presence supports the suggestion that it is difficult to avoid the entrainment of oxide films into a melt during the casting process.

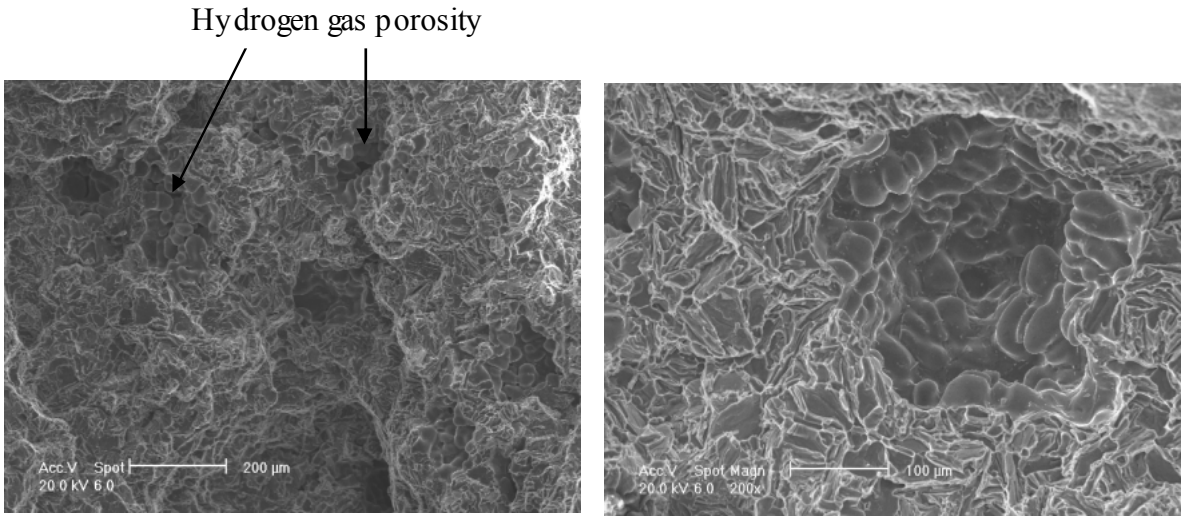

(a) (b)

Figure 4.19 The scanning electron micrograph showing gas porosity on the fracture surfaces obtained from a) the high Fe, high hydrogen and low oxide film casting and b) the low Fe, high hydrogen and low oxide film casting.

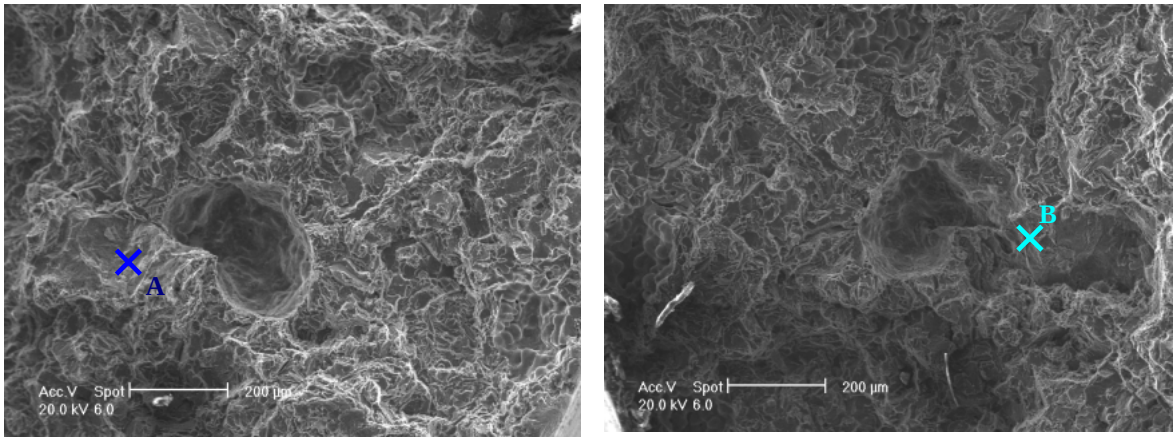

(a) (b)

Figure 4.20 The scanning electron micrograph showing double oxide films on both sides of fracture surfaces obtained from test bar 10 of the high Fe, high hydrogen and low oxide film casting.

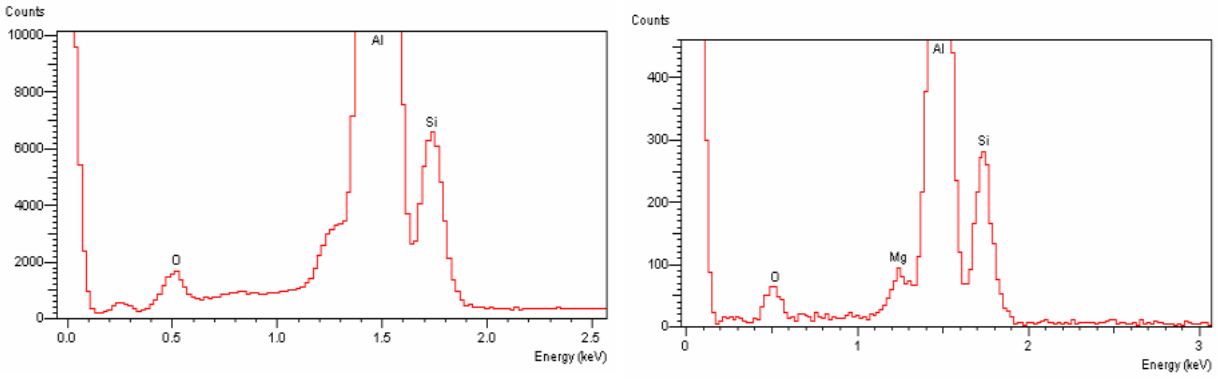

(a) (b)

Figure 4.21 The EDX analysis obtained from points A and B in Figure 4.20.

Figure 4.22 shows the fracture surfaces of test bar 20 obtained from the low Fe, high hydrogen and low oxide film combination. The test bar had low tensile properties (UTS of 261 MPa and elongation of 1.06 %) compared to the mean UTS and mean elongation obtained from this experimental combination (of about 279 MPa and 2.32 % respectively). Figures 4.23a to 4.23d show higher magnification SEM images obtained from fracture surfaces of the test bar and associated EDX analyses are shown in Figures

4.24a and 4.24b; these revealed that the reduction in tensile properties of the test bar was also associated with double oxide film defects. The high magnification image of these oxide film defects have been shown in Figures 4.25a and 4.25b. These images suggested that this oxide film had a finer wrinkled nature, and a thinner thickness, compared to the oxide film found in the high oxide film castings, for example, Figures 4.9a and 4.9b. The EDX analysis result in Figures 4.25c also showed that the oxygen peak of this oxide film was less than that obtained from Figure 4.9c. This suggests that oxide films found in the low oxide film castings was a young oxide film, which is usually defined as formed by surface turbulence during mould filling.

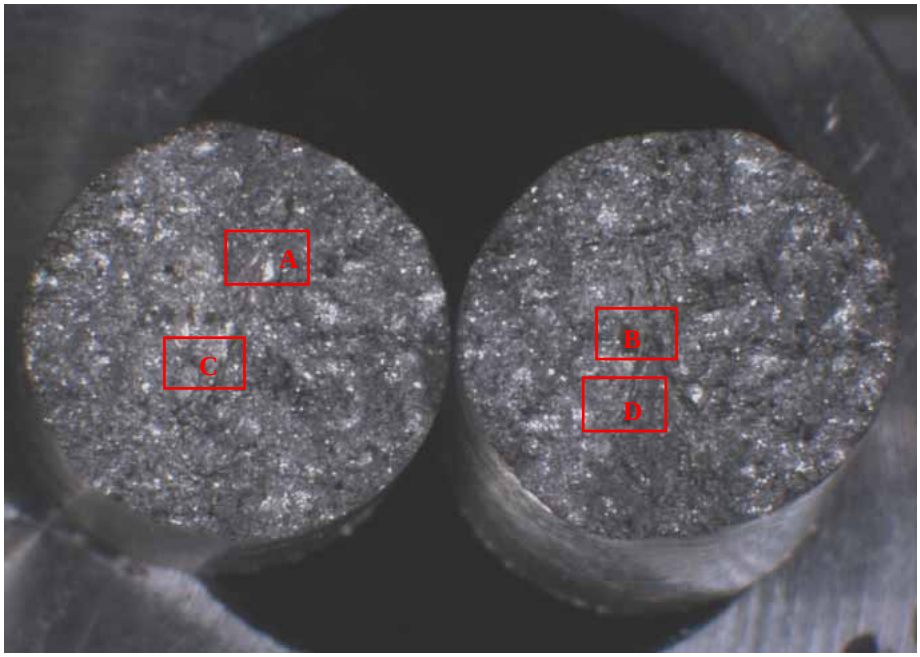

Figure 4.22 Photograph showing the fracture surfaces of test bar 20 obtained from the low Fe, high hydrogen and low oxide film casting.

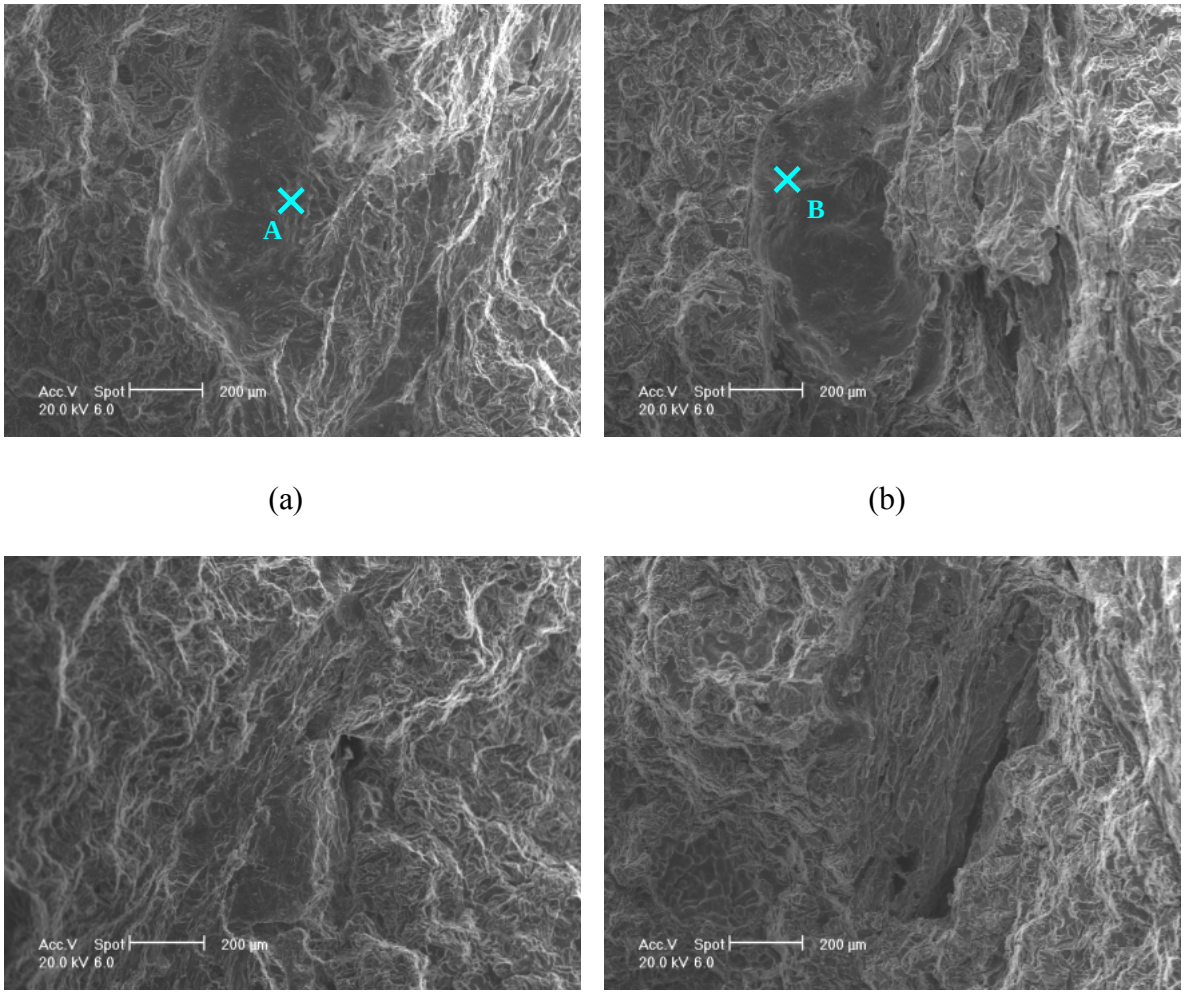

(a) (b)

(c) (d)

Figure 4.23 The scanning electron micrographs showing the close-up images of oxide films on the fracture surfaces from areas A to d in Figure 4.22.

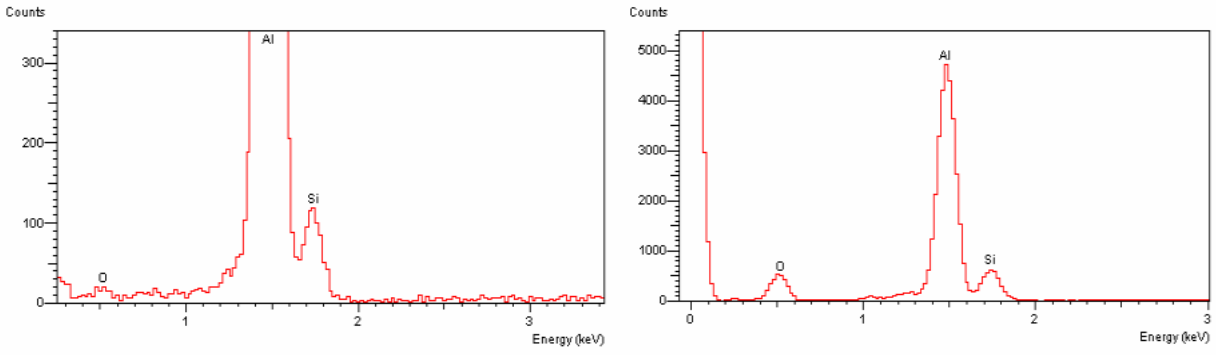

(a) (b)

Figure 4.24 The EDX analysis results obtained from points A and B in Figure 4.23a and 4.23b.

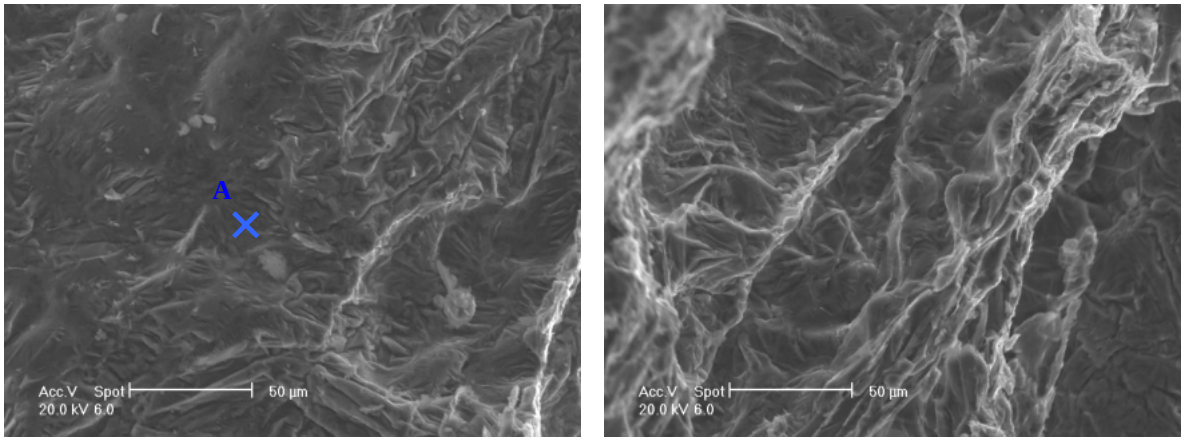

(a) (b)

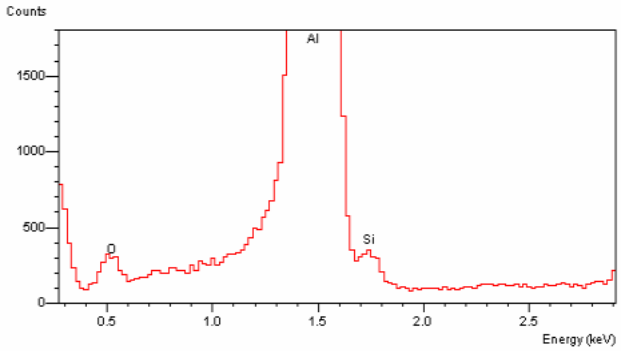

(c)

Figure 4.25 The scanning electron micrographs showing (a) and (b) the young oxide films on the fracture surface of test bar 20 obtained from the low Fe, high hydrogen and low oxide film casting, (c) the EDX analysis result obtained from point A in Figure 4.25a.

In addition, the SEM images of the oxide films on the fracture surfaces also revealed an interaction between oxide films and Fe-rich phases wherein oxide films appeared to be the nucleation sites of Fe-rich phases, as has been suggested elsewhere [Narayanan et al. 1994, Samuel et al. 1998, Cao and Campbell 2001]. Figure 4.26a shows the wrinkled nature of the oxide films observed on the fracture surface of test bar 21 of the low Fe-rich phase, low hydrogen and high oxide film casting. The back-scattered electron image

in Figure 4.26b has revealed Fe-rich particles nucleated onto the wetted under surface of the oxide film. The EDX analysis in Figure 4.27 and the needle-like morphology suggested that the Fe-rich phases nucleated on the oxide films were the β-Al_5FeSi phase. It can be seen that Fe-rich phase appeared to grow following the contours of the wrinkled oxide film. Figures 4.28a and 4.28b show an SEM image and back-scattered electron image respectively, obtained from test bar 10 of the high Fe-rich phase, high hydrogen and high oxide films casting showing more evidence that the oxide film acted as the nucleation site for the β-Al_5FeSi phase. The SEM images also show that the increase in Fe content from 0.1wt% to 0.5 wt % resulted in an increase in Fe-rich phase size from about 10 μm to about 50 μm.

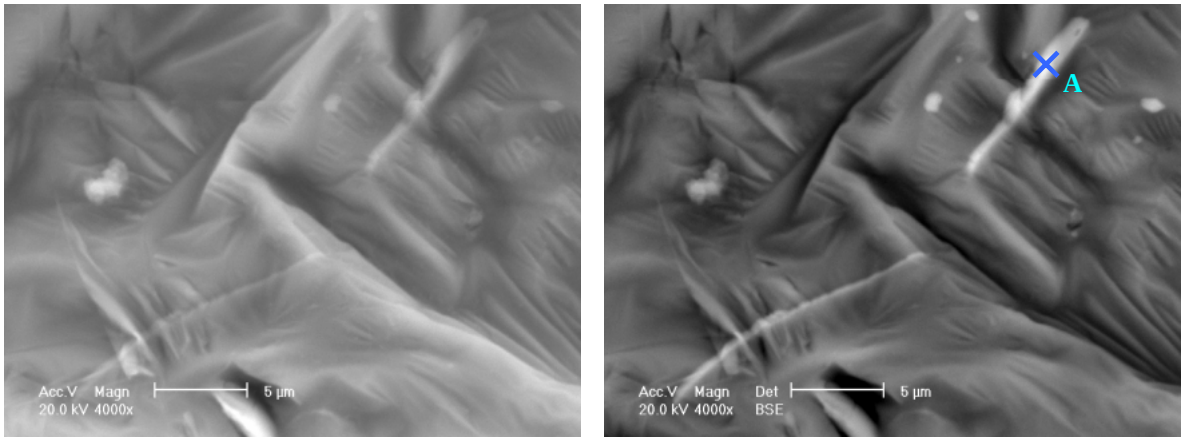

(a) (b)

Figure 4.26 The scanning electron micrographs of test bar 21 obtained from the low Fe-rich phase, low hydrogen and high oxide film casting showing (a) the β-Al_5FeSi phase nucleated onto the wetted side of oxide film (b) the back-scattered image of Figure 4.26a.

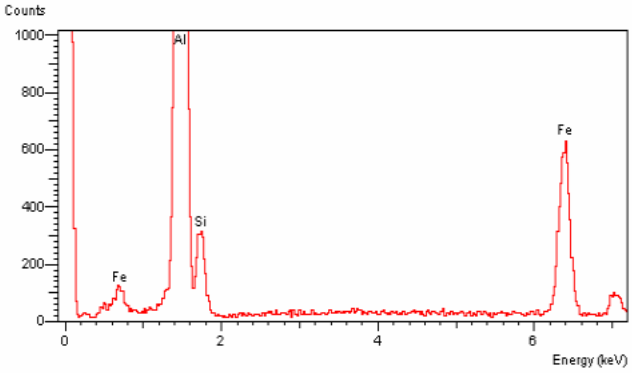

Figure 4.27 The EDX analysis obtained from point A in Figure 4.26b.

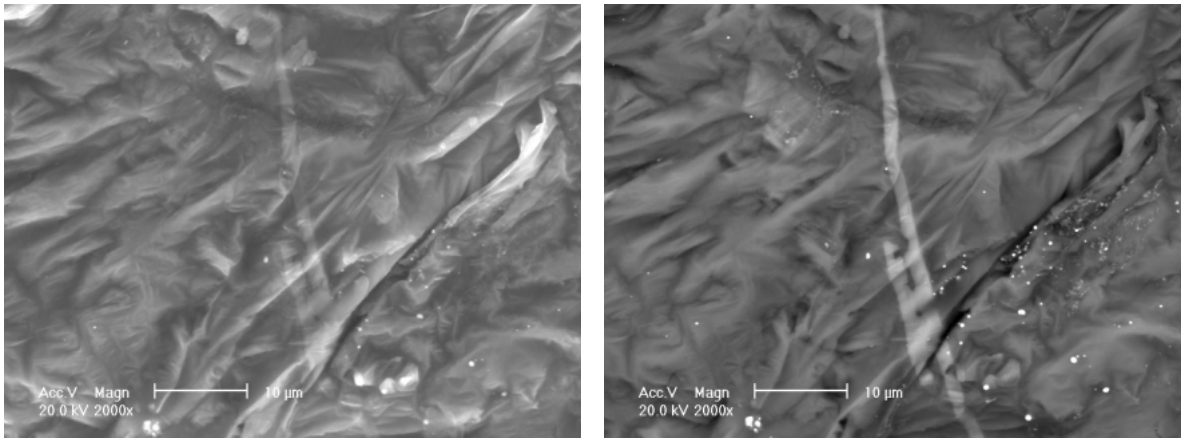

(a) (b)

Figure 4.28 The scanning electron micrographs of of test bar 10 obtained from the high Fe, high hydrogen and high oxide film casting showing (a) the β-Al_5FeSi phase nucleated onto the wetted side of oxide film (b) the back-scattered image obtained from Figure 4.28a.

4.1.4 Weibull analysis

The tensile property results were further analyzed to investigate the distribution of the data. The distribution histograms of ultimate tensile strength (UTS) and percent elongation are shown in Figures 4.29a to 4.29h and 4.30a to 4.30h respectively. These diagrams demonstrated that the data from the best property casting, with a combination of low Fe-rich phase, low hydrogen gas and low oxide film, was the only set of data that seemed to have a normal distribution, particularly so in the case of the UTS data. Increasing the Fe content, hydrogen gas and oxide films resulted in increased scatter of the data and a change in the data to a non-normal distribution (e.g. Figures 4.29b and 4.30b). Therefore, the single defect Weibull distribution was used to describe a scatter in tensile properties of castings [Green and Campbell 1993].

Figures 4.31a and 4.31b show graphs of cumulative probability of fracture versus UTS and Weibull plots obtained from the UTS data respectively. The graphs of probability of fracture versus elongation and Weibull plots obtained from the elongation data have been shown in Figures 4.32a and 4.32b respectively. The slope of a linear line drawn through the set of data in the Weibull plots is the so-called Weibull modulus. The greater the value of the Weibull modulus the narrower the range of tensile properties. The Weibull Moduli and R values, which show the matching of the fitted line and data (the closer to 1 for the R value, the better fit of the line), determined from Figures 4.31b and 4.32b are given in Table 4.5.

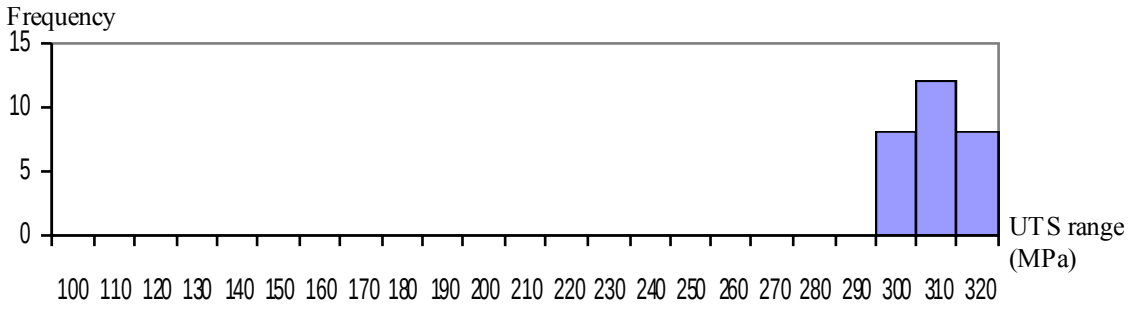

(a) low Fe, low H_2, low oxide film

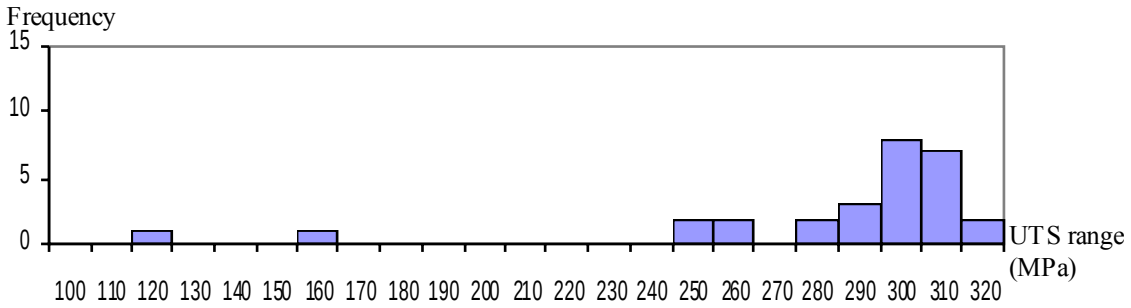

(b) low Fe, low H_2, high oxide film

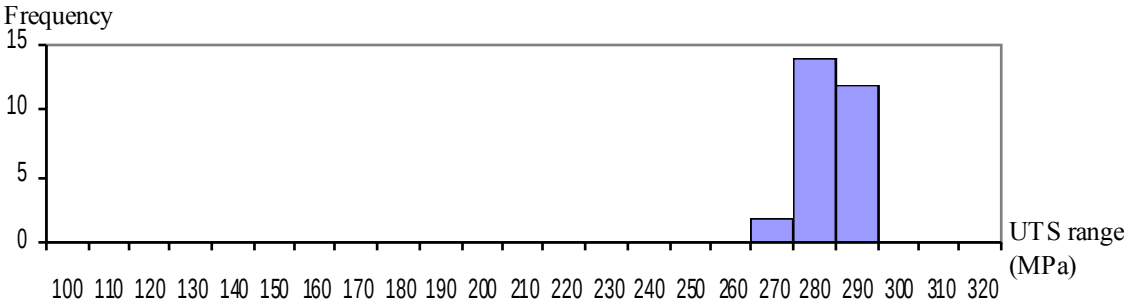

(c) low Fe, high H_2, low oxide film

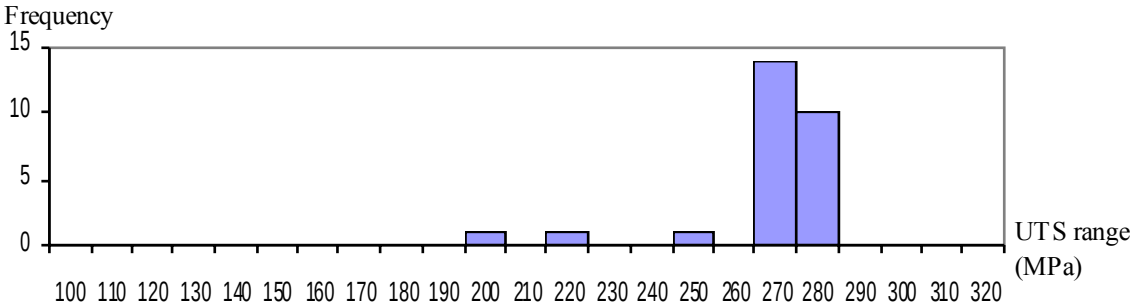

(d) low Fe, high H_2, high oxide film

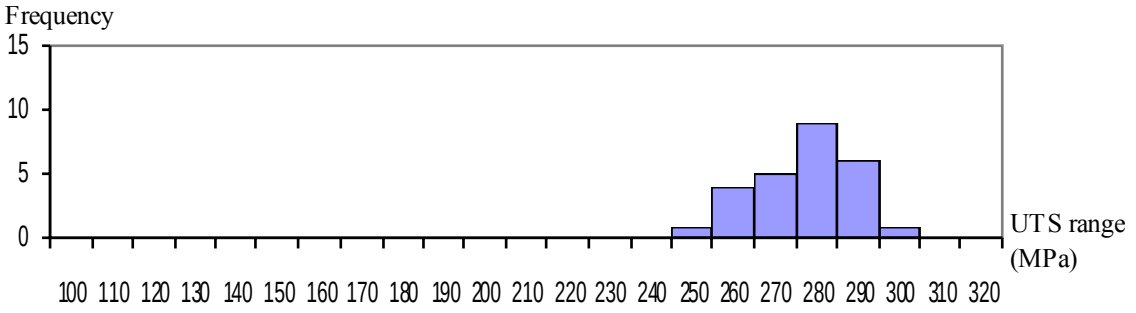

(e) high Fe, low H_2, low oxide film

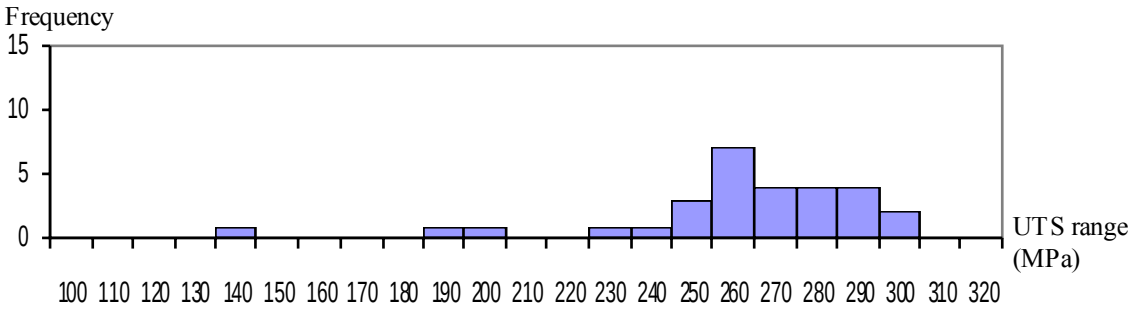

(f) high Fe, low H_2, high oxide film

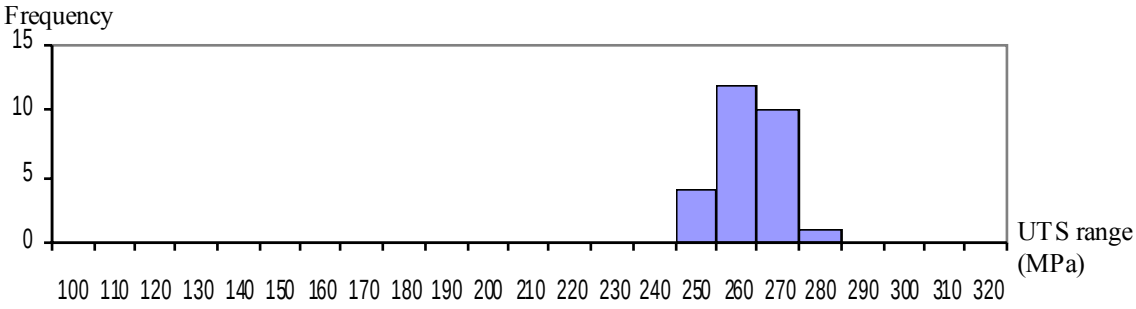

(g) high Fe, high H_2, low oxide film

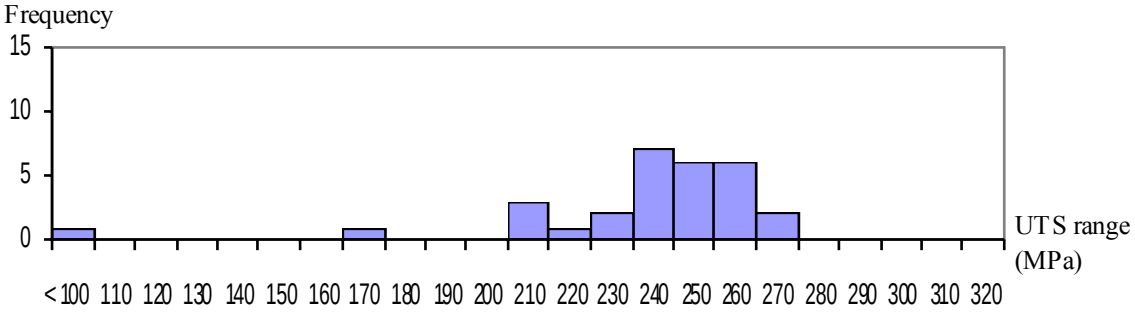

(h) high Fe, high H_2, high oxide film

Figure 4.29 Frequency plots of ultimate tensile strength (UTS).

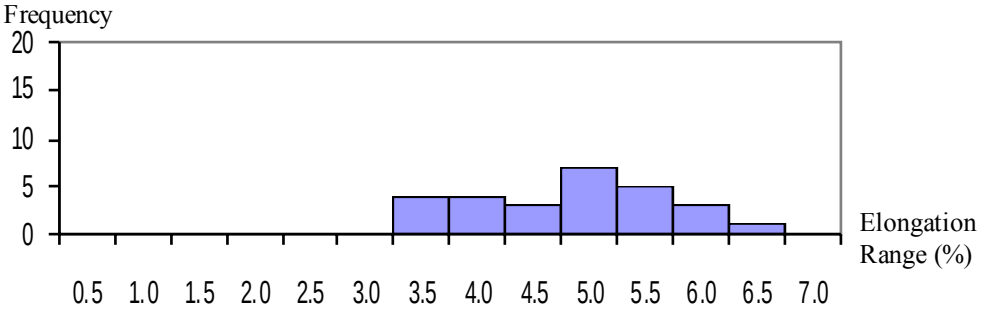

(a) low Fe, low H_2, low oxide film

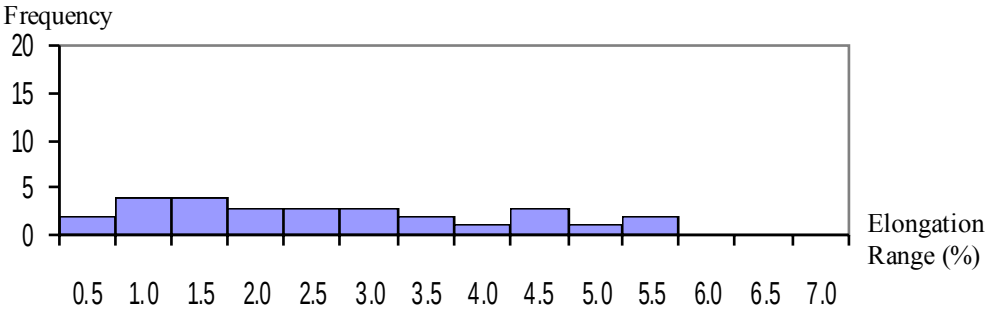

(b) low Fe, low H_2, high oxide film

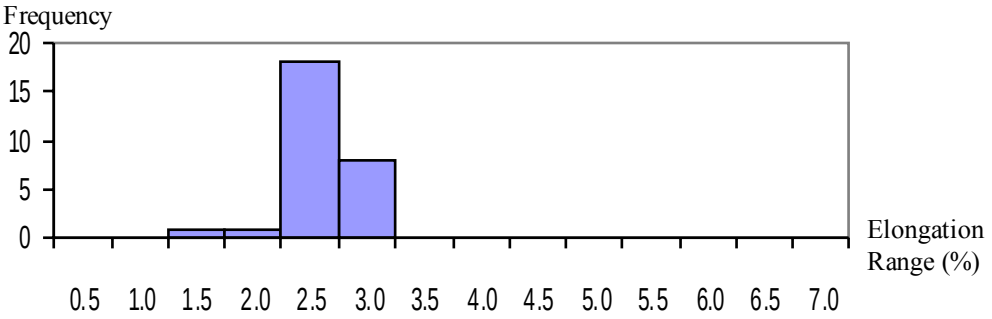

(c) low Fe, high H_2, low oxide film

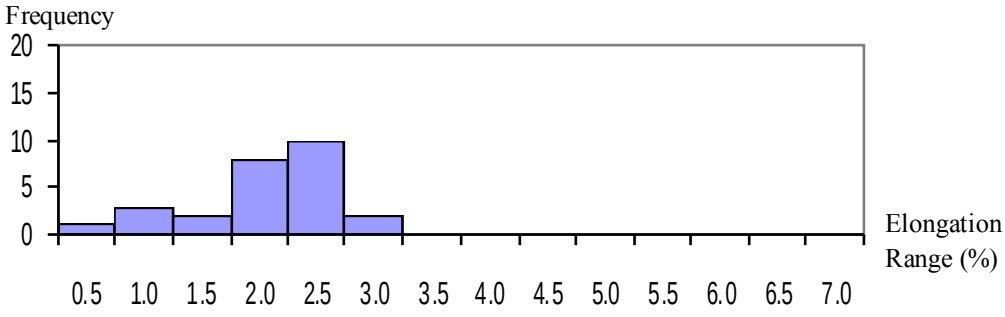

(d) low Fe, high H_2, high oxide film

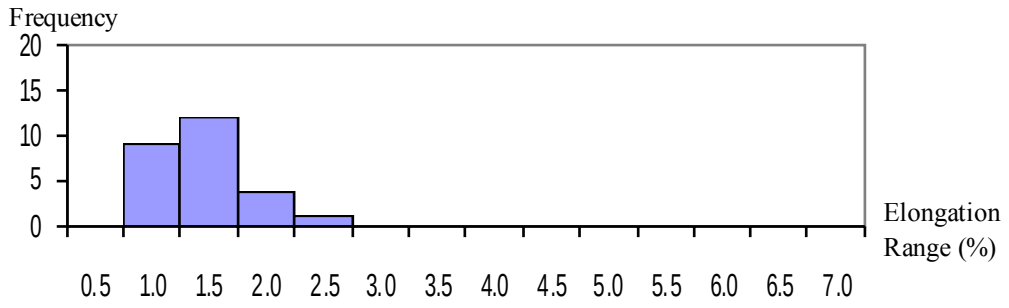

(e) high Fe, low H_2, low oxide film

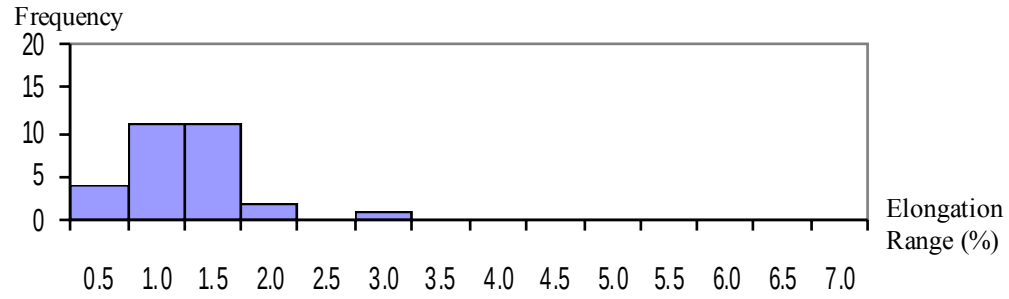

(f) high Fe, low H_2, high oxide film

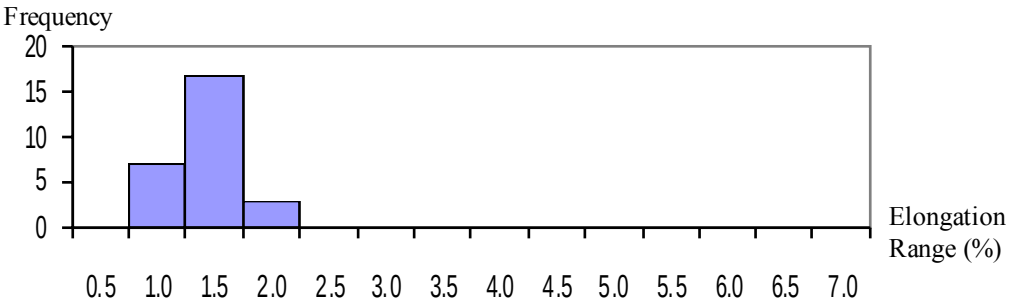

(g) high Fe, high H_2, low oxide film

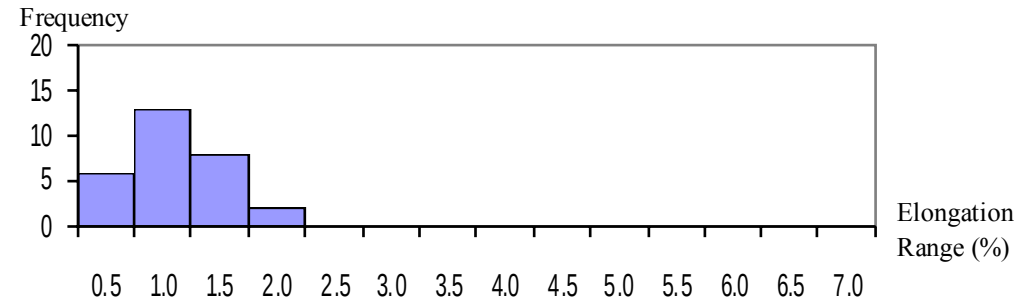

(h) high Fe, high H_2, high oxide film

Figure 4.30 Frequency plots of percent elongation.

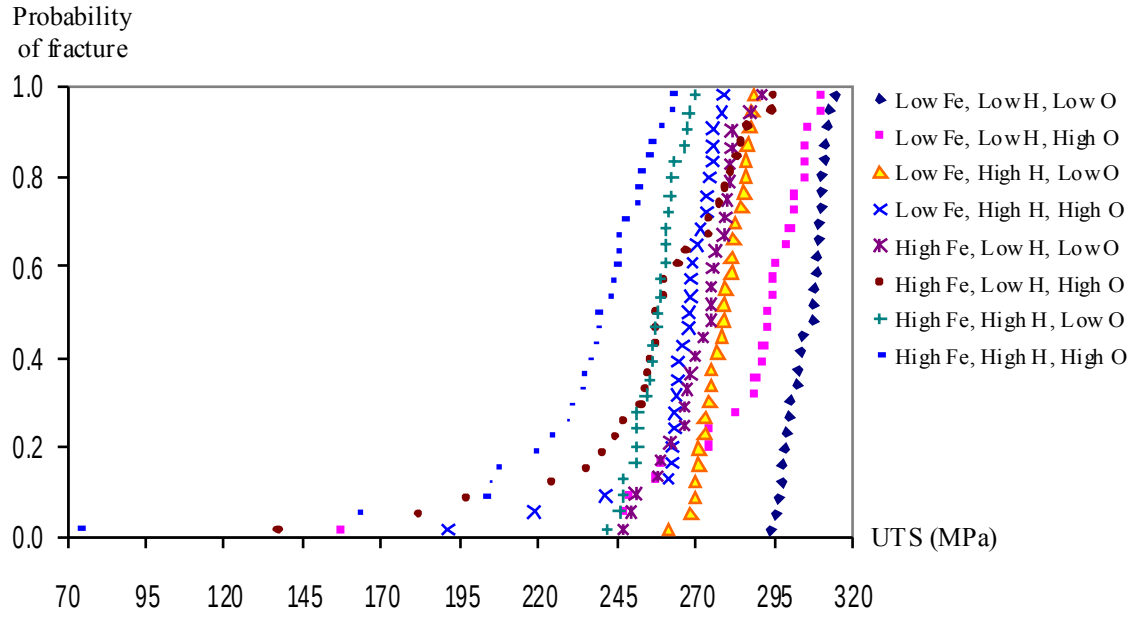

(a)

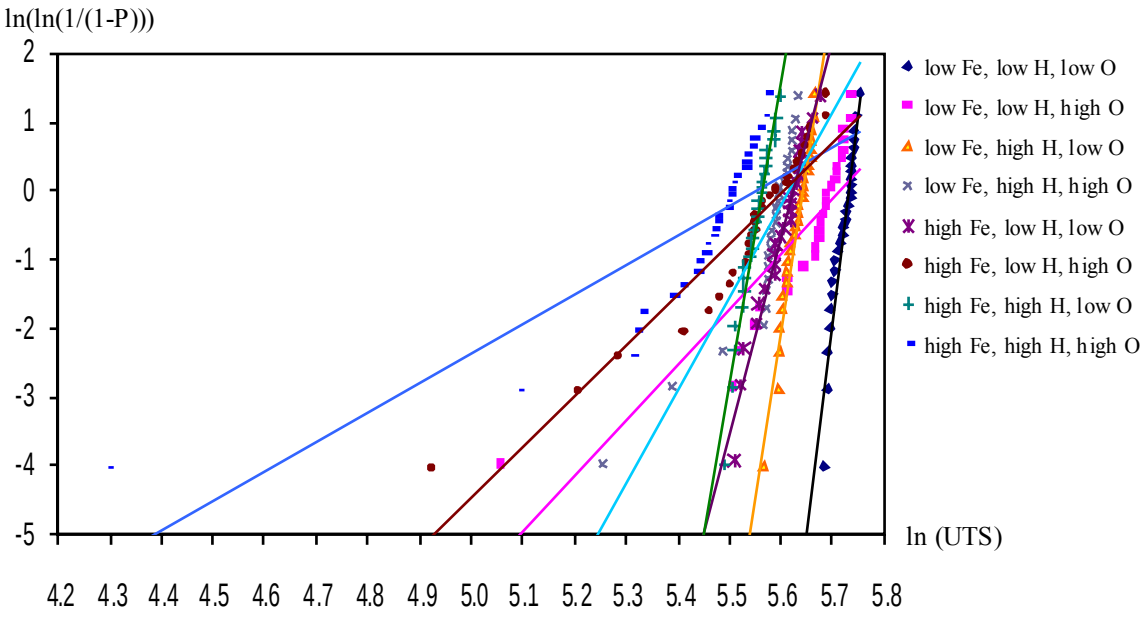

(b)

Figure 4.31 The graphs showing (a) cumulative plots (b) Weibull plots of ultimate tensile strength (UTS) data of the castings.

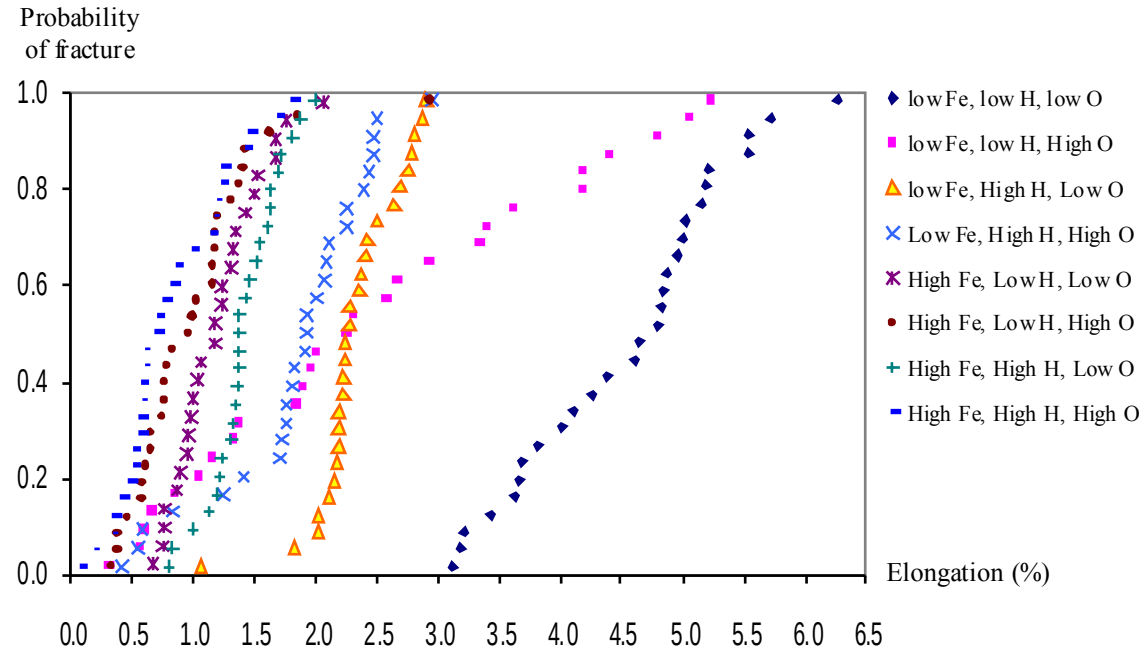

(a)

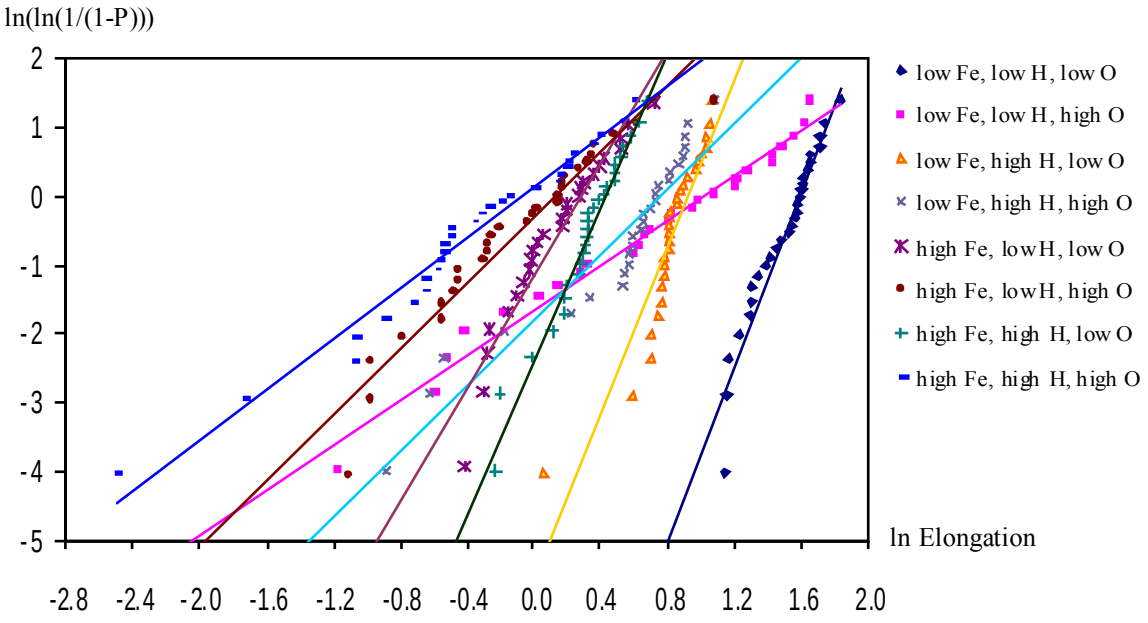

(b)

Figure 4.32 The graphs showing (a) cumulative plots (b) Weibull plots of percent elongation data of the castings.

Table 4.5 Weibull modulus values obtained from the Weibull plots of ultimate tensile strength (UTS) (Figure 4.31b) and percent elongation (Figure 4.32b).

Combination	UTS Weibull modulus	R	Elongation Weibull modulus	R
low Fe, low H_2, low oxide film	55.5	0.96	5.77	0.97
low Fe, high H_2, low oxide film	43.9	0.98	5.32	0.92
high Fe, high H_2, low oxide film	39.8	0.98	5.01	0.99
high Fe, low H_2, low oxide film	25.8	0.99	4.10	0.97
low Fe, high H_2, high oxide film	11.7	0.86	2.12	0.95
low Fe, low H_2, high oxide film	7.0	0.86	1.63	0.99
high Fe, low H_2, high oxide film	6.5	0.89	2.16	0.95
high Fe, high H_2, high oxide film	3.7	0.79	1.63	0.99

The Weibull plots illustrated that the low oxide film, low hydrogen gas and low Fe-rich phase combination had the highest Weibull modulus, (i.e., produced the least scatter in the results), while the high oxide film, high hydrogen gas and high Fe-rich phase combination had the lowest Weibull modulus, (the greatest scatter in values). As shown in Table 4.5, the presence of oxide film increased the variability of the casting properties most since the Weibull modulus was markedly lower in every experiment that contained a high oxide film content in the case of both tensile strength and elongation results. The Fe-rich phase also produced a noticeable change due to a decrease in the Weibull modulus, for example in the low hydrogen and low oxide film content castings the presence of Fe-rich phase resulted in a reduction of the Weibull modulus of about 30 for UTS and 1.7 for elongation. The hydrogen porosity appeared to make only a slight difference in Weibull modulus in this experiment, for example increasing hydrogen content from 0.1 to 0.45 ml/100 g metal decreased the Weibull modulus by about 12 for UTS and 0.5 for elongation in the low Fe-rich phase and low oxide film castings.

However, the Weibull plots suggested that the tensile properties data, particularly the UTS data, obtained from the high oxide film combinations did not plot linearly as would be expected of data distributed in the form of a single defect Weibull distribution. For example, in the Weibull plot of the UTS data obtained from the high Fe, high hydrogen and high oxide film castings (the blue dots in Figure 4.31b), most data was distributed as

a linear line except the low UTS values (test bars 7 and 21). Table 4.5 also shows that oxide film defects influenced the distribution of tensile properties by decreasing the R values of the Weibull plots obtained from the high oxide film castings. For example, the R value obtained from the high Fe, high hydrogen and high oxide film test bars was only 0.79. This indicated that, apart from the Fe-rich phase, there was another defect type influencing the failure mechanism of the test bars. The SEM images obtained from the fracture surfaces of test bar 7 (Figures 4.16) showed the presence of large double oxide film defects and it therefore was likely to be a cause of failure. The observation of fracture surfaces of the test bars in the high oxide film casting supported this suggestion since they showed that all lower values test bars contained extensive double oxide film defects (e.g. Figures 4.6, 4.10 and 4.13).

Figures 4.33a and 4.33b show the Weibull distribution diagram of the UTS data obtained from the high oxide film combinations experiments. It can be seen that if the data is plotted as two separate lines, with low UTS values and high UTS values, better linear fits can be obtained. This suggested that the distribution of the UTS data with the high oxide film content could be divided into two trend-lines by the different failure mechanisms, first was the Weibull distribution associated with the normal failure mechanism, caused by brittle particles in the casting, and the second was the Weibull distribution associated with the failure due to large oxide film defects (the lower UTS values). Therefore the Weibull Moduli and R values of the UTS data obtained from the high oxide film castings were redetermined considering only the failure caused by oxide film defects and these have been shown in Table 4.6.

This shows that the presence of oxide film defects resulted in a remarkable decrease in the UTS Weibull modulus compared to those in the low oxide film castings (see Table 4.5). For example in the low Fe and low hydrogen content test bars, the increase in oxide film content made the UTS Weibull modulus decrease by about 51. The low Weibull modulus suggests that the range of UTS data was wide. Therefore the variety of shape and size of oxide films introduced into the casting, particularly in the unfiltered mould, (the high oxide content castings), that contained large oxide film defects, played a major role in the reduction in the reliability of the castings.

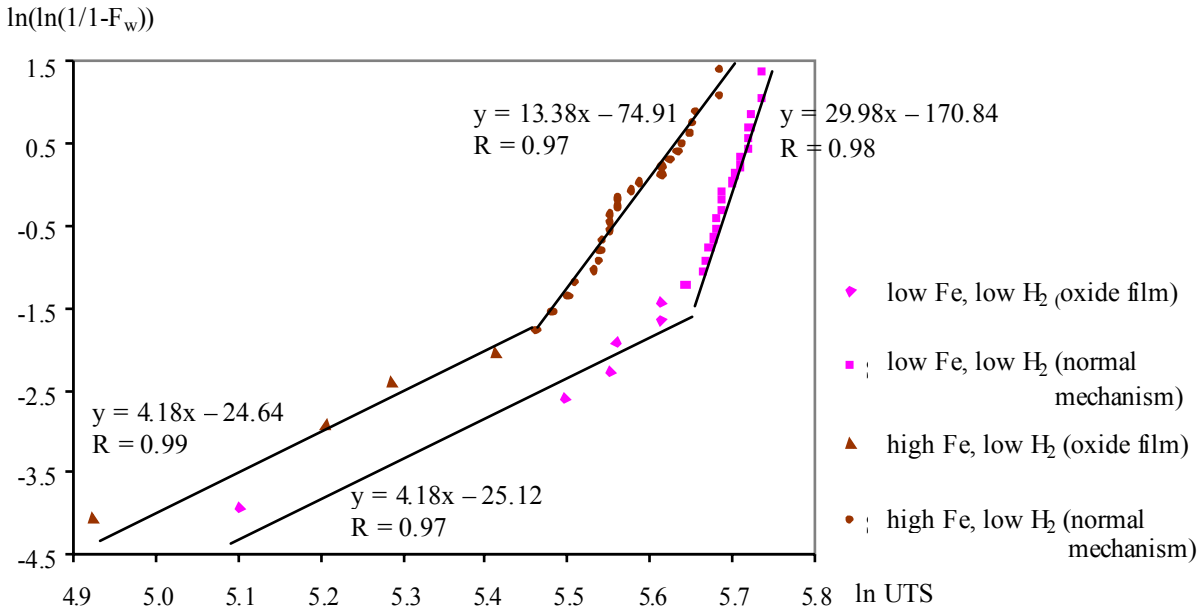

(a)

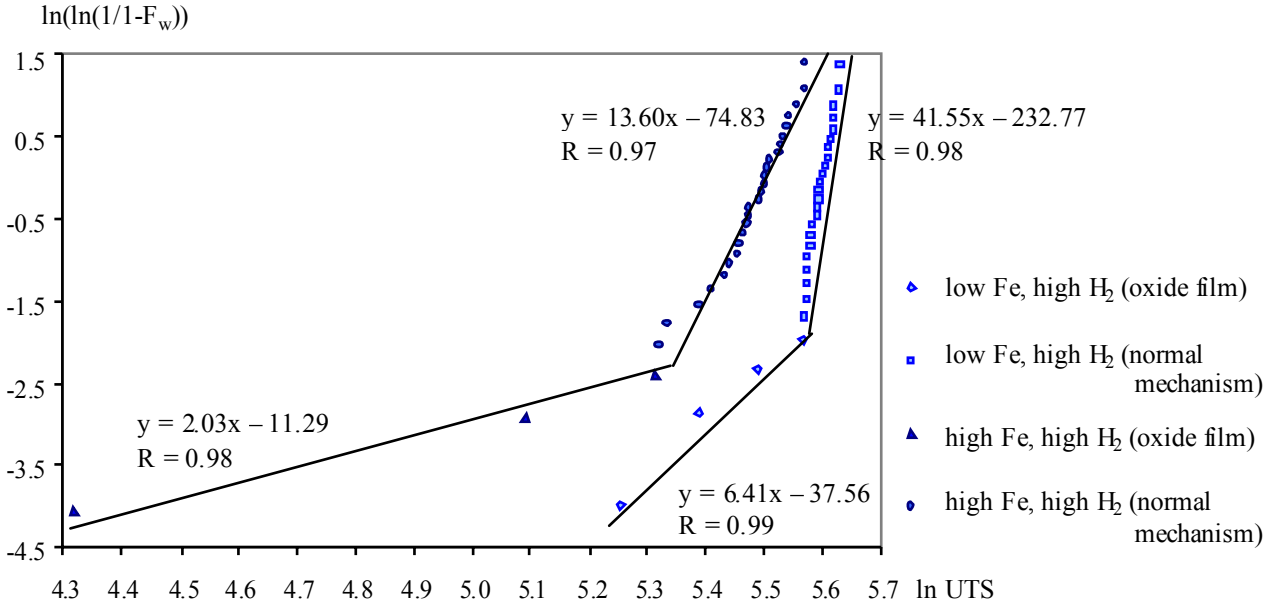

(b)

Figure 4.33 The Weibull plots of the UTS data obtained from the high oxide film castings showing two trend-lines classified by the failure mechanism of the test bars (normal mechanism and caused by large double oxide film defects)

Table 4.6 Weibull modulus values of ultimate tensile strength (UTS) obtained from the Weibull plots in Figures 4.33a, 4.33b.

Combination	UTS Weibull modulus	R
low Fe, low H_2, high oxide film	4.2	0.98
low Fe, high H_2, high oxide film	6.4	0.98
high Fe, low H_2, high oxide film	4.2	0.97
high Fe, high H_2, high oxide film	2.0	0.97

The effects of Fe-rich phase, hydrogen porosity, oxide films and their interactions on the Weibull modulus were estimated by Yates' algorithm. Tables 4.7 and 4.8 show the Yate's algorithm calculation obtained from the UTS Weibull modulus and elongation Weibull modulus respectively. Pareto diagrams illustrating the relative effects of three defects and their interactions have been shown in Figure 4.34a and 4.34b respectively. Oxide film (column C) had the greatest effect on the Weibull modulus, (about 37 on the Weibull modulus of the UTS and about 3.2 on the elongation Weibull modulus). The effect of Fe-rich phase on the UTS and elongation Weibull modulus was about 10 and 0.5 respectively (column A) while the hydrogen porosity (column B) had a negligible effect on the Weibull modulus in this experiment. The diagrams suggested interactions between Fe-rich phase, hydrogen porosity and oxide films (column ABC) that influenced the Weibull modulus the most in this experiment, (the effects on UTS Weibull modulus and elongation Weibull modulus were 8 and 0.6 respectively). It can be seen that an interaction between Fe-rich phase and oxide films (column AC) also effect on the distribution of tensile properties by increasing UTS Weibull modulus and elongation Weibull modulus about 7 and 0.5 respectively.

Table 4.7 The effect of Fe-rich phase, hydrogen porosity, oxide film and their interactions on UTS Weibull modulus using Yate's algorithm.

	total	1	2	3	estimate of effect
(1)	55.5	81.4	165.0	181.8	45.5
A (effect of Fe-rich phase)	25.8	83.7	16.8	-38.2	-9.5
B (effect of gas porosity)	43.9	8.4	-33.8	2.4	0.6
AB	39.8	8.4	-4.4	21.2	5.3
C (effect of oxide film)	4.2	-29.7	2.3	-148.2	-37.1
AC	4.2	-4.1	0.1	29.4	7.4
BC	6.4	0.0	25.5	-2.2	-0.6
ABC	2.0	-4.4	-4.4	-29.9	-7.5

Table 4.8 The effect of Fe-rich phase, Hydrogen porosity, Oxide film and their interactions on elongation Weibull modulus using Yate's algorithm.

	total	1	2	3	estimate of effect
(1)	5.77	9.87	20.20	27.74	6.94
A (effect of Fe-rich phase)	4.10	10.33	7.54	-1.94	-0.49
B (effect of gas porosity)	5.32	3.79	-1.98	0.42	0.11
AB	5.01	3.75	0.04	0.34	0.08
C (effect of oxide film)	1.63	-1.67	0.46	-12.66	-3.17
AC	2.16	-0.31	-0.04	2.02	0.51
BC	2.12	0.53	1.36	-0.50	-0.13
ABC	1.63	-0.49	-1.02	-2.38	-0.60

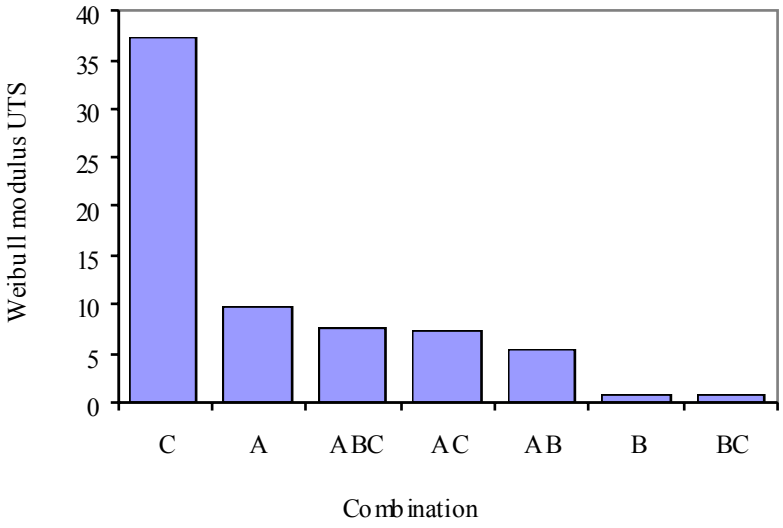

(a)

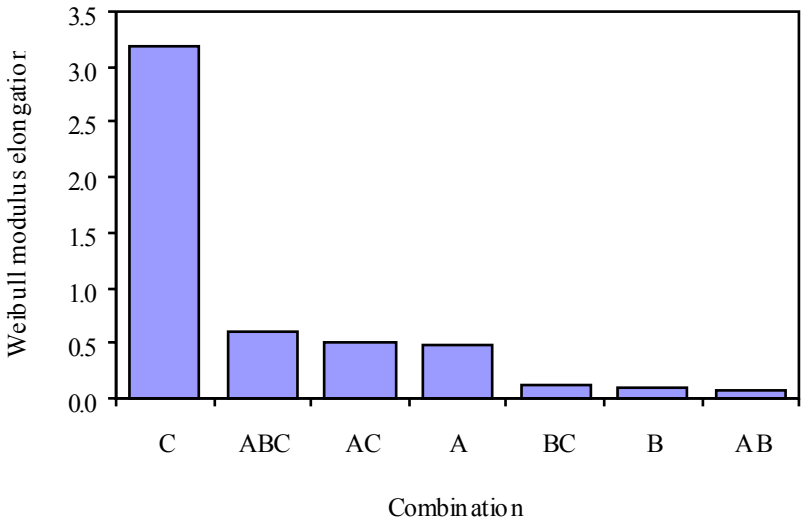

(b)

Figure 4.34 Pareto diagrams showing (a) the effects of three defects and their interrelationships on the UTS Weibull modulus and (b) on the elongation Weibull modulus of the castings (A = Fe-rich phase, B= hydrogen porosity, C = oxide film)

4.1.5 Castings microstructures

The runner bars and heat-treated tensile test bars obtained from each combination of the experimental castings were examined by optical microscopy. The main microstructural features observed were α-Al dendrites, Al-Si eutectic, and various Fe-rich intermetallic compounds such as α-$Al_{15}Fe_3Si_2$, β-Al_5FeSi, and π-$Al_8FeMg_3Si_6$. Figure 4.35 shows microstructures from the low Fe content alloy obtained from a cross sections of the runner bar (as-cast). Figure 4.36 shows SEM images of a microstructure obtained from the low Fe, low hydrogen and low oxide film combination. The EDX analysis shown in Figure 4.37 demonstrated that the most frequent Fe-rich phase observed in the low Fe content castings (0.1 wt%) was π-$Al_8FeMg_3Si_6$, usually occurring as a Chinese script-like or indefinite shape. Figure 4.38 shows the microstructure of a low Fe, low hydrogen and high oxide film content alloy obtained from a cross-section of a heat-treated test bar. Figures 4.39a and 4.39b show SEM images with EDX analysis result shown in Figure 4.40, which shows that the microstructure of the castings was changed by the heat treatment to produce finer/more rounded Al-Si eutectic phases and a small platelet or needle-like morphology of β-Al_5FeSi phase instead of the π-$Al_8FeMg_3Si_6$ phase.

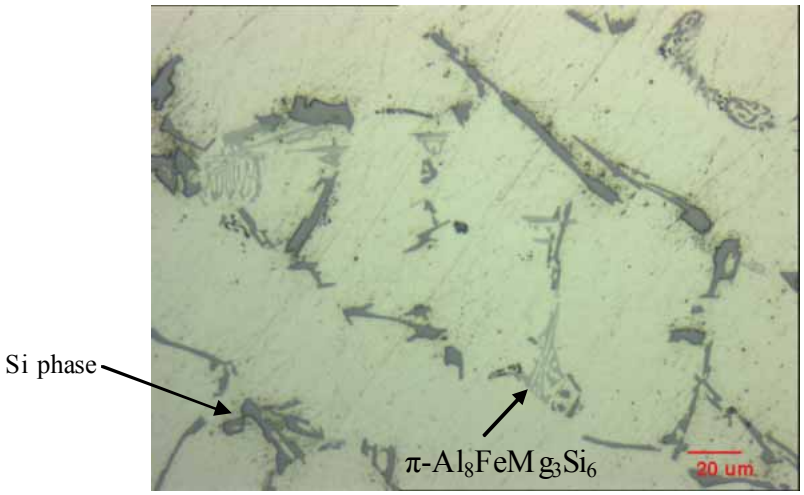

Figure 4.35 Optical micrograph of cross section of runners obtained from the low Fe, high hydrogen and high oxide film castings showing its microstructures.

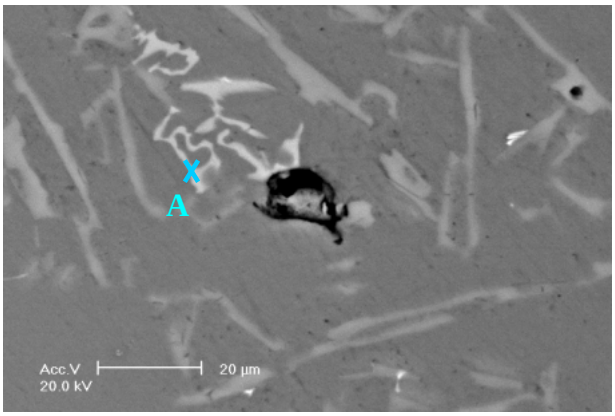

Figure 4.36 The scanning electron micrographs of cross section of runner bar (as-cast) obtained from low Fe, low hydrogen and low oxide film casting showing its microstructure.

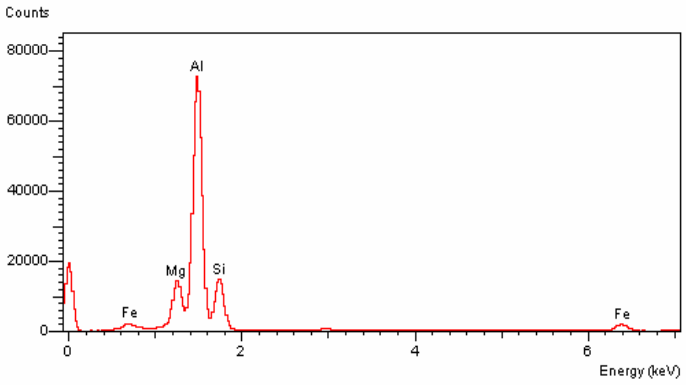

Figure 4.37 The EDX analysis result obtained from point A in figure 4.36.

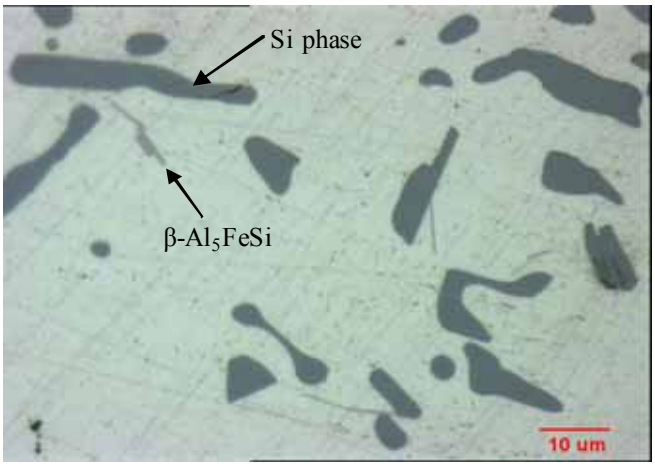

Figure 4.38 Optical micrograph of cross section of heat-treated test bars obtained from low Fe, low hydrogen and high oxide film casting showing its microstructure.

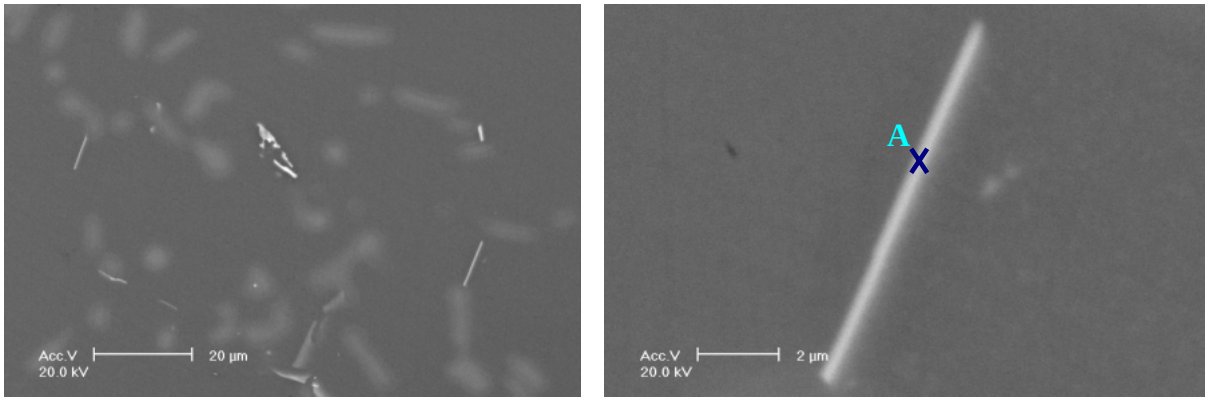

(a) (b)

Figure 4.39 The scanning electron micrographs of heat-treated test bar obtained from low Fe, low hydrogen and high oxide film casting showing (a) microstructure of the casting (b) the close-up observation of β-Al_5FeSi phase from figure 4.39a

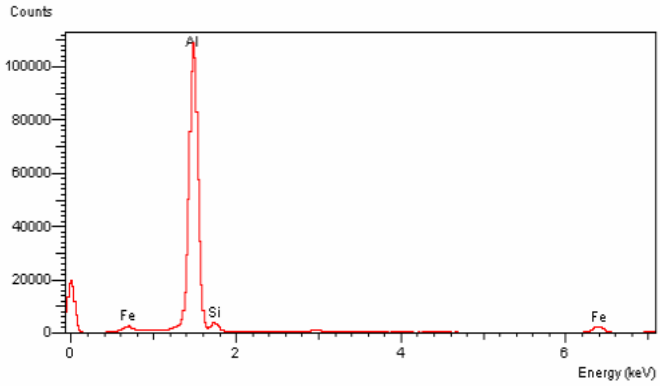

Figure 4.40 The EDX analysis result obtained from point A in figure 4.39b.

Figure 4.41 shows a typical microstructure of a high Fe content casting. The Fe-rich intermetallic compounds were clearly apparent and the most frequent Fe-rich phase was a chunky β-Al_5FeSi platelet. After heat treatment, the β-Al_5FeSi phases developed into thinner large platelets or a needle-like morphology as shown in Figure 4.42.

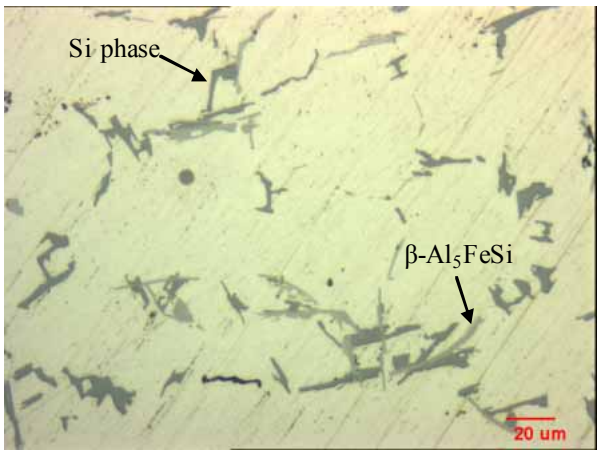

Figure 4.41 Optical micrograph of cross section of runner bar (as-cast) obtained from high Fe, low hydrogen and high oxide film casting showing its microstructure.

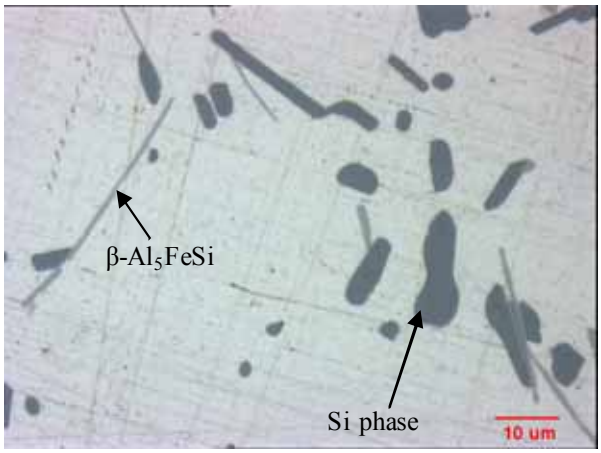

Figure 4.42 Optical micrograph of cross section of heat-treated test bars obtained from high Fe, high hydrogen and low oxide film casting showing its microstructure.

Figures 4.43a to 4.43h show microstructures of samples obtained from the cross sections of heat-treated test bars of each of the 8 combinations of the defects in the castings. As shown in the microstructures, porosity was the main defect observed in the castings. In the low hydrogen content alloys (0.1 ml/100 g metal), porosity formed as microporosity,

which has the size less than 100 µm, and located in the interdendritic regions as shown in Figures 4.43a to 4.43d. When hydrogen content increased to 0.45 ml/100g metal, it directly influenced the size of pore and resulted in the presence of gas porosity in the castings as shown in Figures 4.43e to 4.43h.

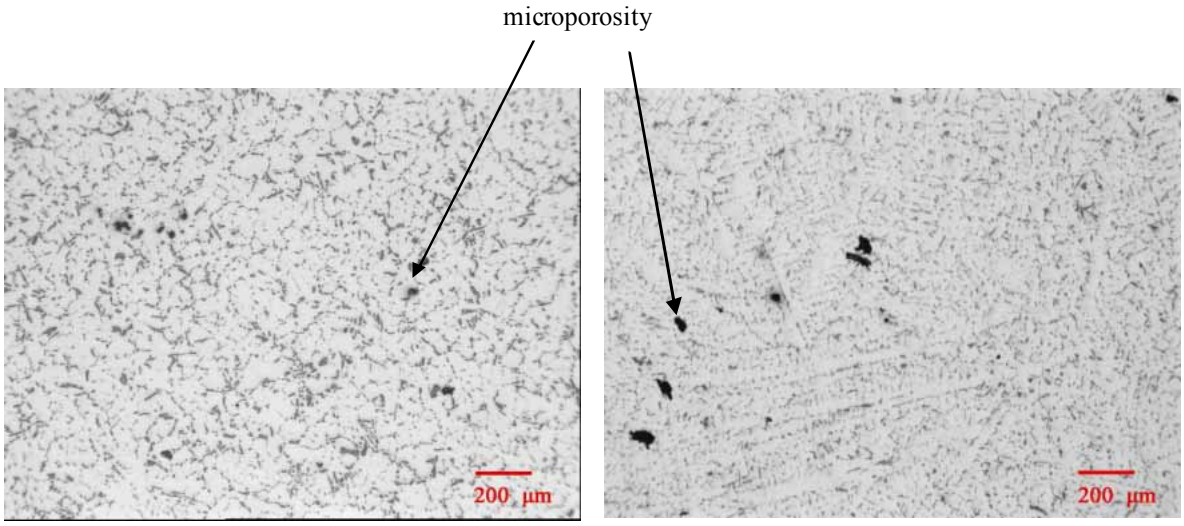

(a) low Fe, low H_2 and low oxide film

(b) low Fe, low H_2 and high oxide film

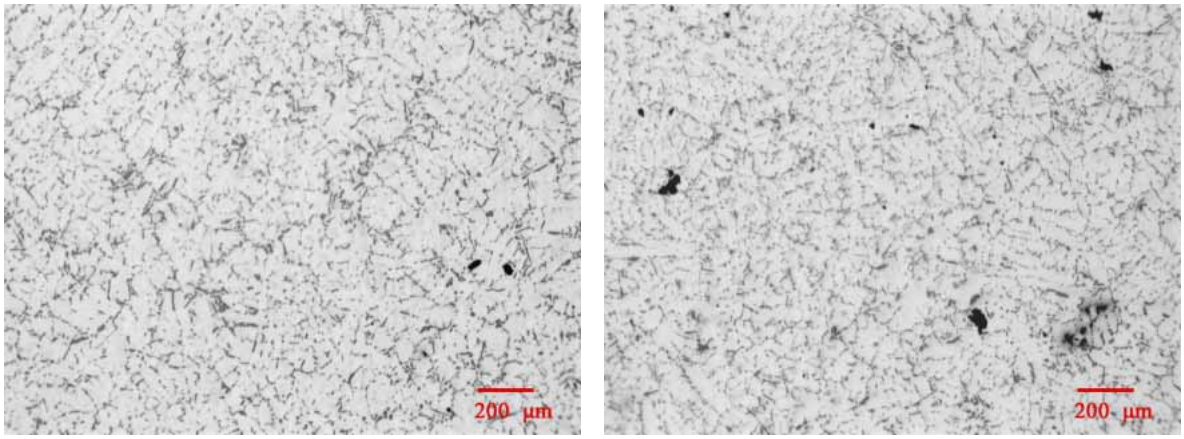

(c) high Fe, low H_2 and low oxide film

(d) high Fe, low H_2 and high oxide film

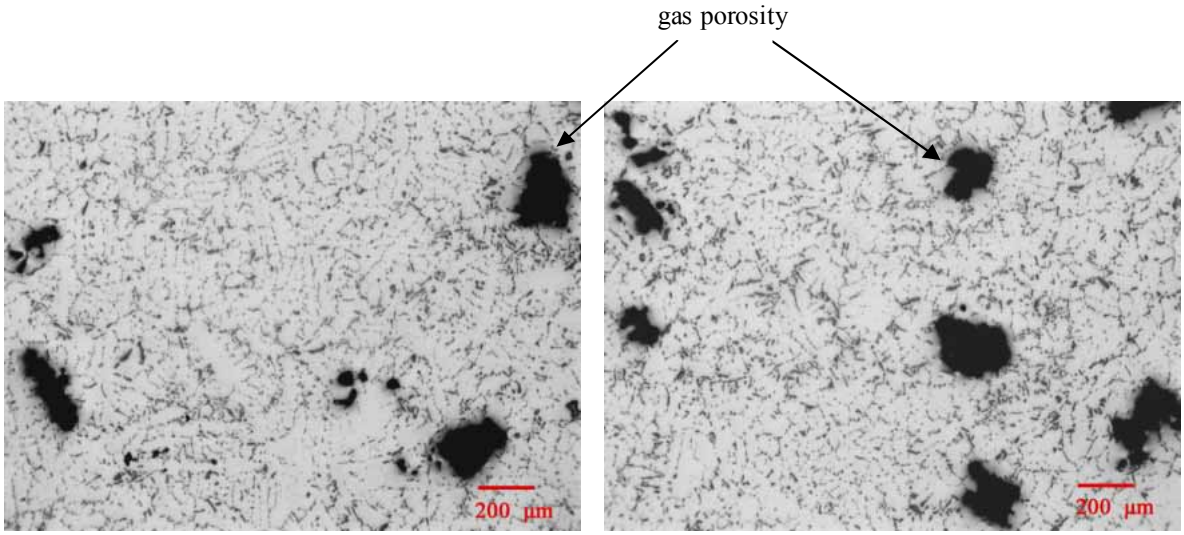

(e) low Fe, high H_2 and low oxide film

(f) low Fe, high H_2 and high oxide film

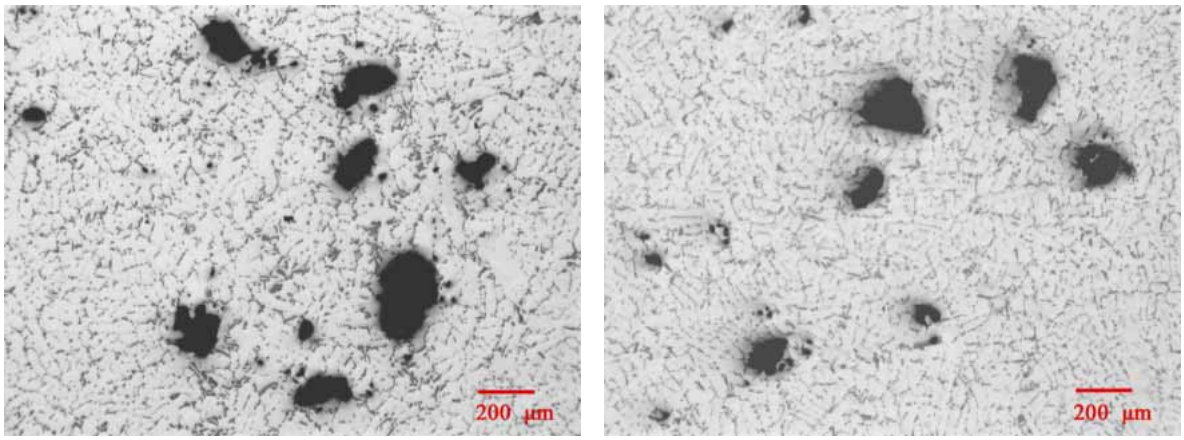

(g) high Fe, high H_2 and low oxide film

(h) high Fe, high H_2 and high oxide film

Figure 4.43 Optical micrographs showing microstructures of castings obtained from 8 experimental combinations.

About 20 pores of each casting combination were observed by the SEM. The results suggested an interaction between oxide films and porosity since more than 90% of observed pores contained oxide films in their interior surfaces. Figure 4.44 shows an example of gas porosity obtained from the runner bar of the high oxide film, high

hydrogen and high Fe casting and the EDX analysis results of this pore have been shown in Figures 4.45a to 4.45c. These clearly show that there were fragments of oxide films at the surface of the pore. Figure 4.46 show another example of microporosity that had the presence of oxide films at its surface obtained from the low oxide film, low hydrogen and low Fe casting and the associated EDX analysis results has been shown in Figure 4.47. These results therefore suggested that the oxide film played an important role in the formation of porosity in castings, and might act as an initiator of pore formation. However, some pores that did not contain oxide films were also found in this experiment, (less than 10% of observed pores), and all of them were microporosity (i.e. below 100 μm in size). Figure 4.48 shows the SEM image of microporosity obtained from the high Fe, low hydrogen and low oxide film casting and the EDX analysis results in Figure 4.49 shows that there was no oxide films detect in the interior.

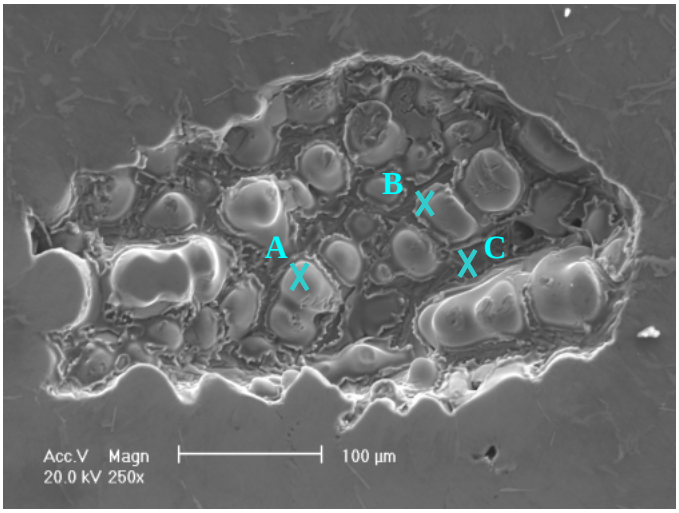

Figure 4.44 The scanning electron micrographs showing oxide films at the interior surface of gas porosity obtained from the high Fe-rich phase, high hydrogen gas and high oxide film casting.

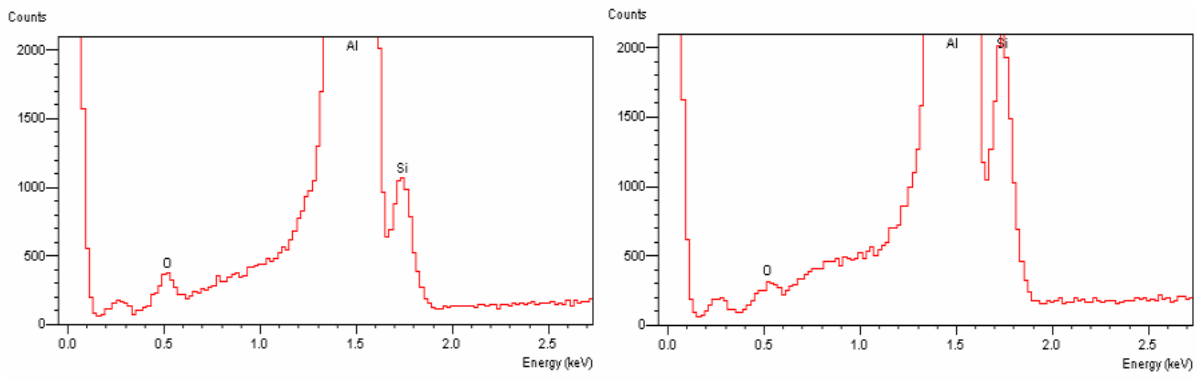

(a) (b)

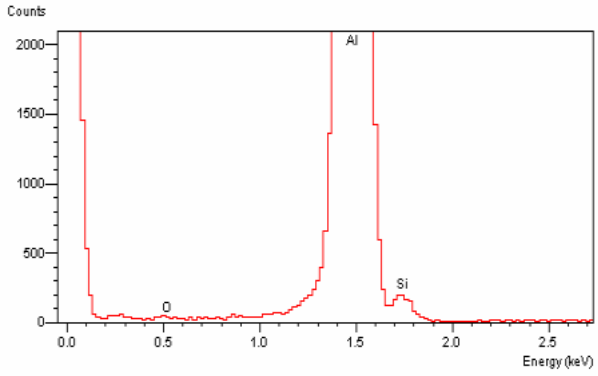

(c)

Figure 4.45 The EDX analysis results obtain from points A to C in Figure 4.44.

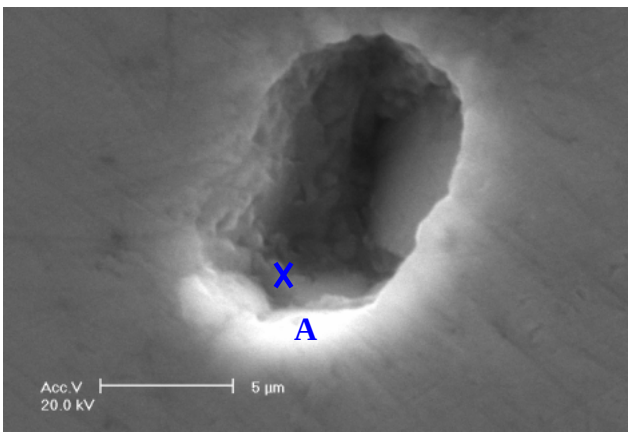

Figure 4.46 The scanning electron micrographs of cross section of the runner bar obtained from low Fe, low hydrogen and low oxide film casting showing microporosity contained oxide film at the internal surface.

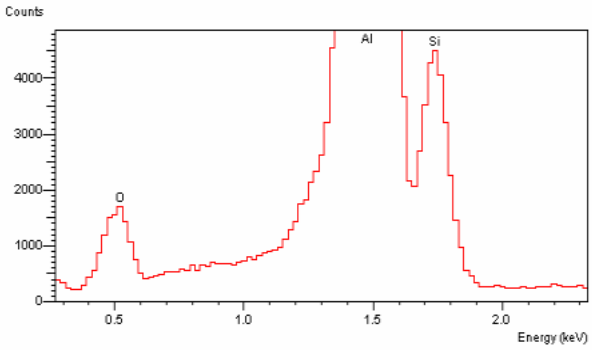

Figure 4.47 The EDX analysis results obtained from point A in Figure 4.46.

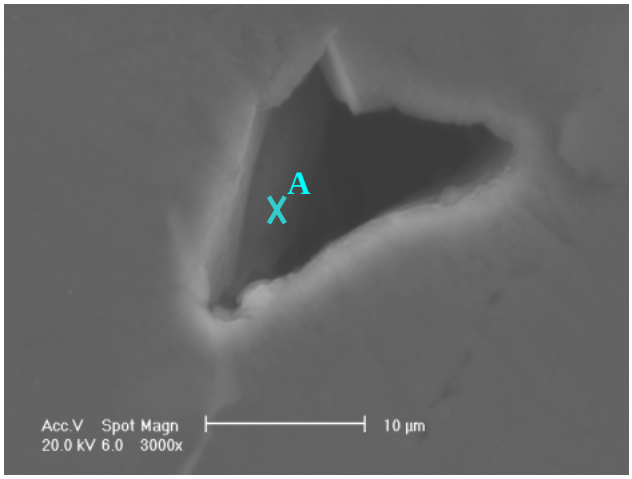

Figure 4.48 The scanning electron micrographs of cross section of the runner bar obtained from high Fe, low hydrogen and low oxide film casting showing microporosity with no oxide film in its interior.

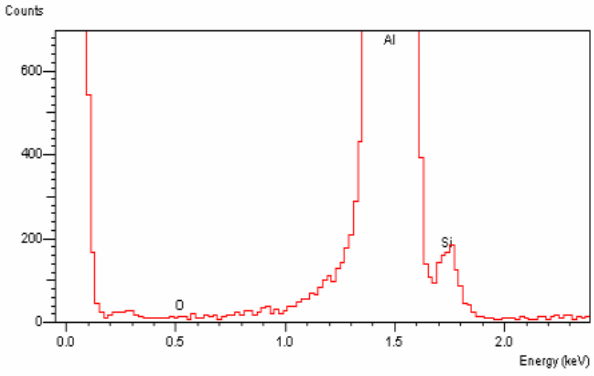

Figure 4.49 The EDX analysis results obtained from point A in Figure 4.48.

Figures 4.50a to 4.50d obtained from the test bar of a low Fe, low hydrogen and high oxide film casting show another type of defect observed in the castings. This was an extensive network of pores with a crack-like morphology, occasionally found in the unfiltered castings. The SEM images from this defect in Figures 4.51a and 4.51b, and the EDX analysis results in Figures 4.52a to 4.52f revealed that this defect was a double oxide film defect that was folded by the surface turbulence of the liquid metal. The tangled oxide films submerged in the melt became a network of crack-like defects in the casting.

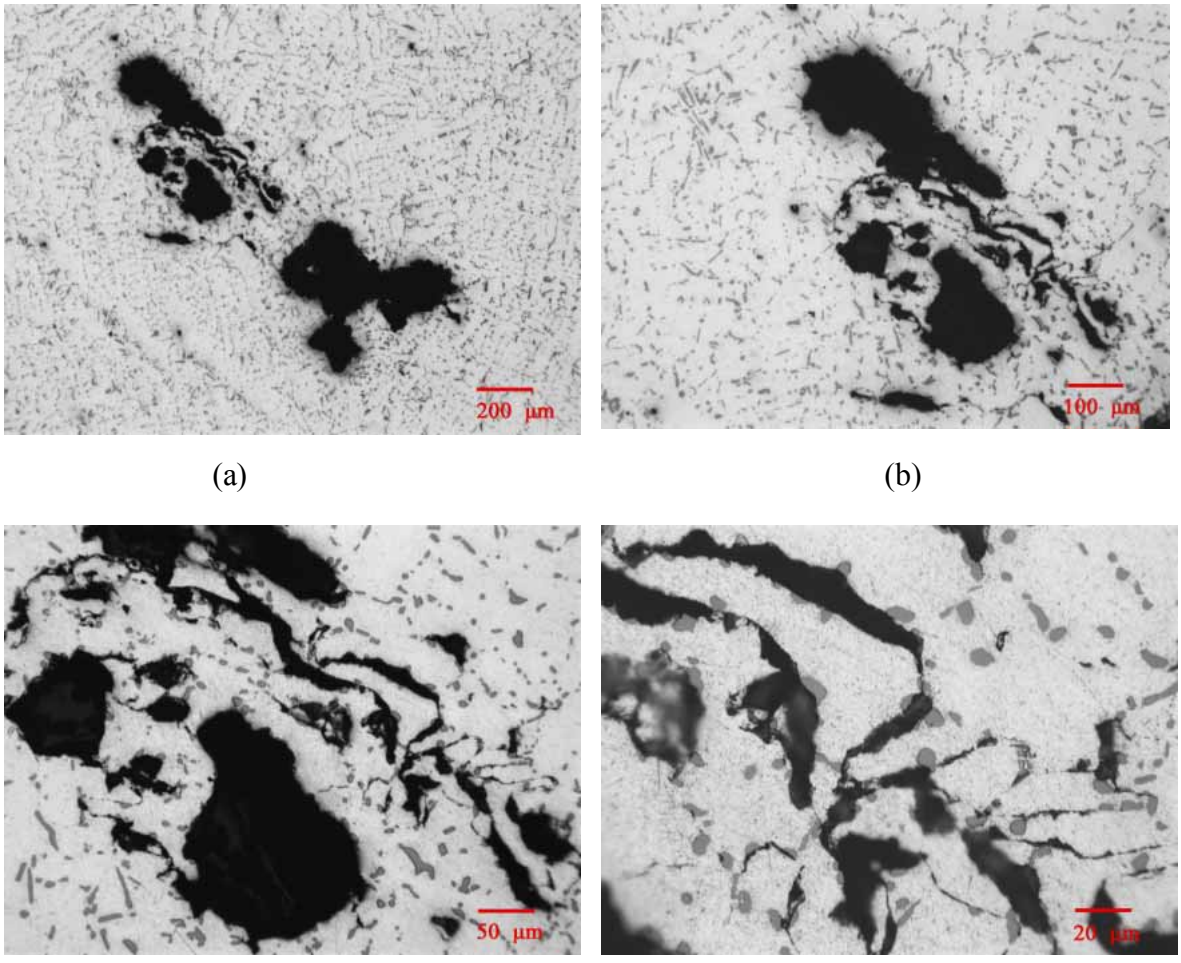

(a) (b)

(c) (d)

Figure 4.50 Optical micrograph showing the crack-like defects with different magnification obtained from low Fe, high hydrogen and high oxide film casting.

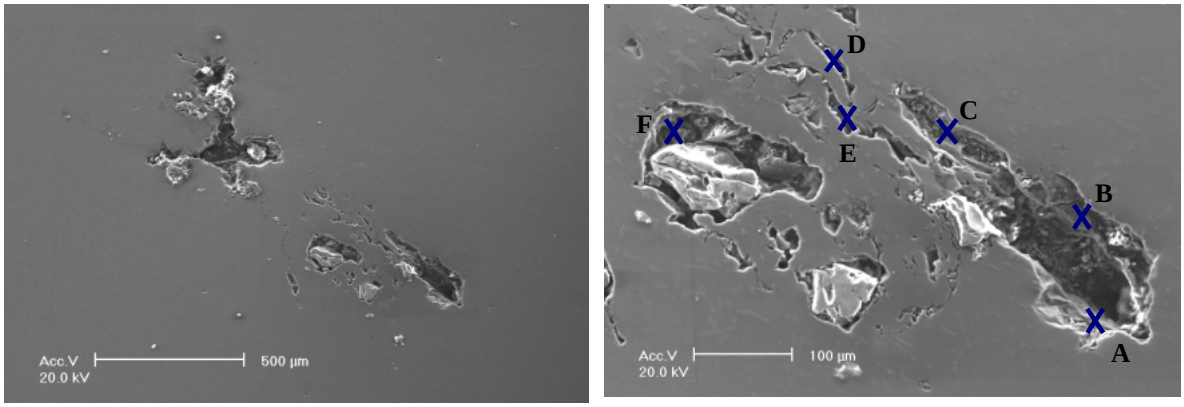

(a) (b)

Figure 4.51 The scanning electron micrographs of heat-treated test bar obtained from low Fe, low hydrogen and high oxide film casting showing (a) oxide film network in the casting (b) the close-up observation of oxide film cracks from figure 4.51a.

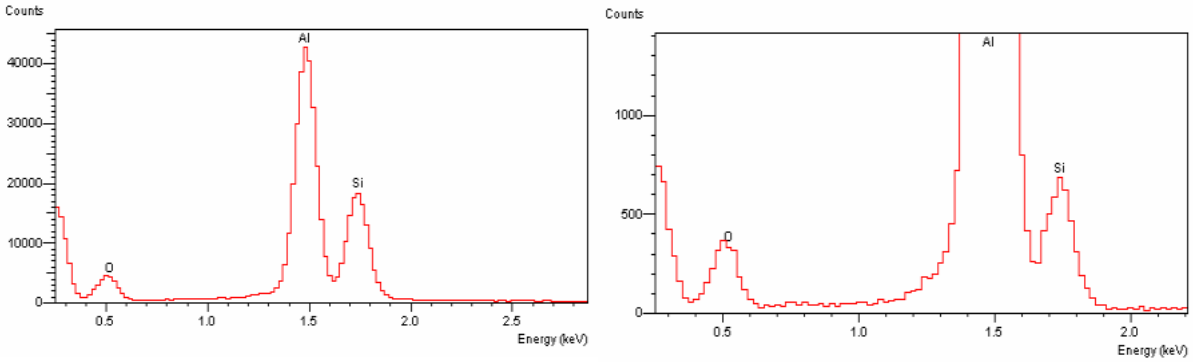

(a) (b)

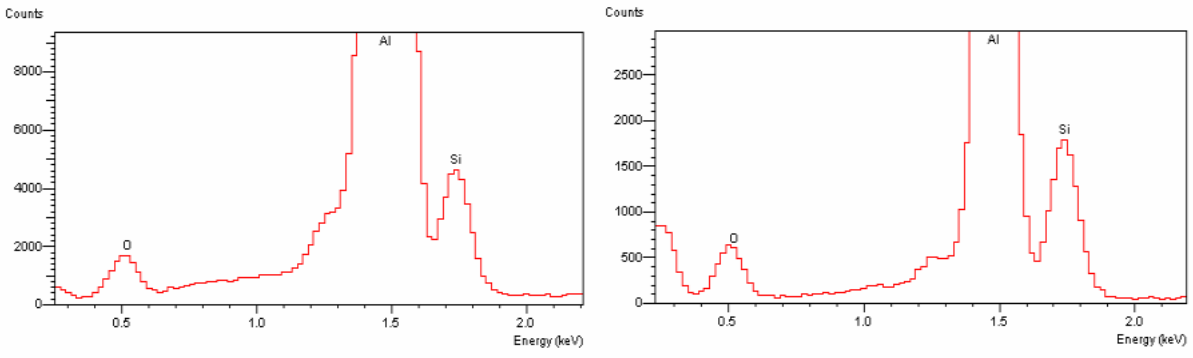

(c) (d)

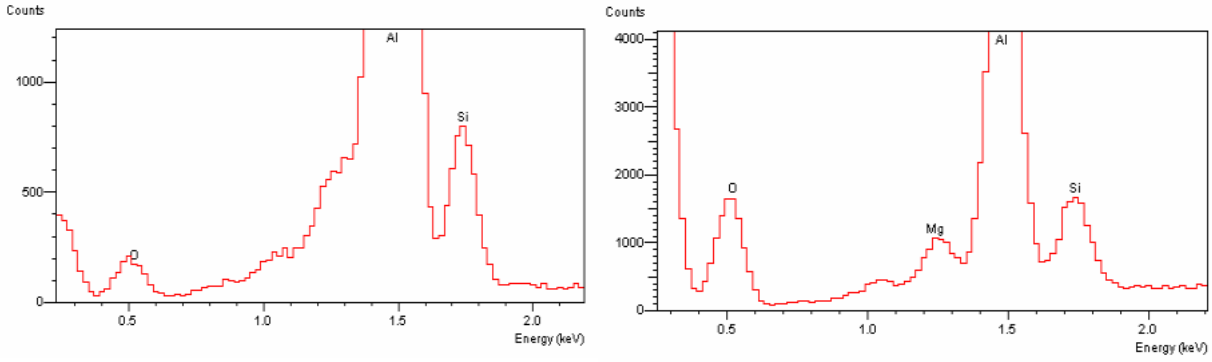

(e) (f)

Figure 4.52 The EDX analysis results obtained from points A to F in figure 4.51b.

Figures 4.53a and 4.53b show other extensive crack-like defects obtained from the test bar of a low Fe, high hydrogen and high oxide film casting. Figures 4.54a to 4.54c show higher magnification images of these defects and Figures 4.55a to 4.55d show the EDX analysis results obtained from these defects. These results also showed that these crack-like defects were double oxide films.

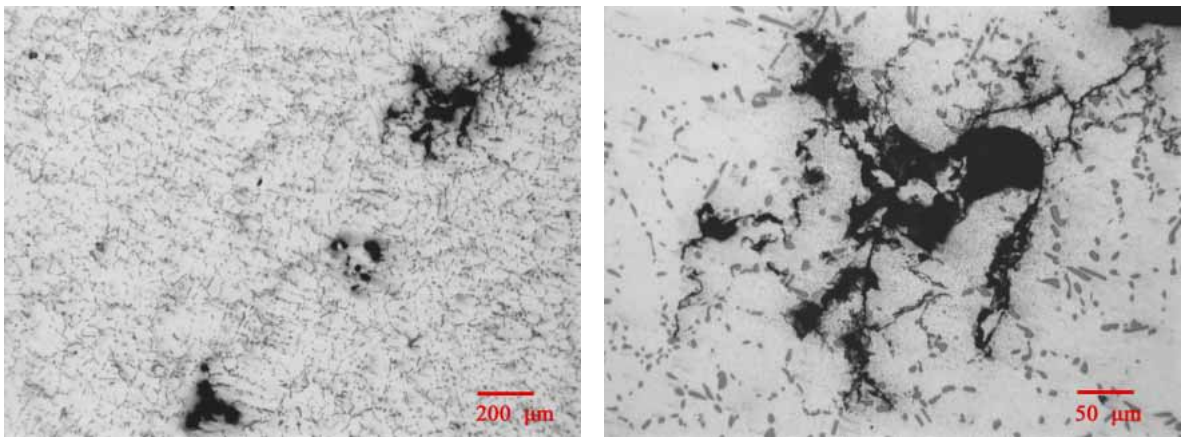

(a) (b)

Figure 4.53 Optical micrograph obtained from low Fe, high hydrogen and high oxide film casting showing the crack-like defects with different magnification.

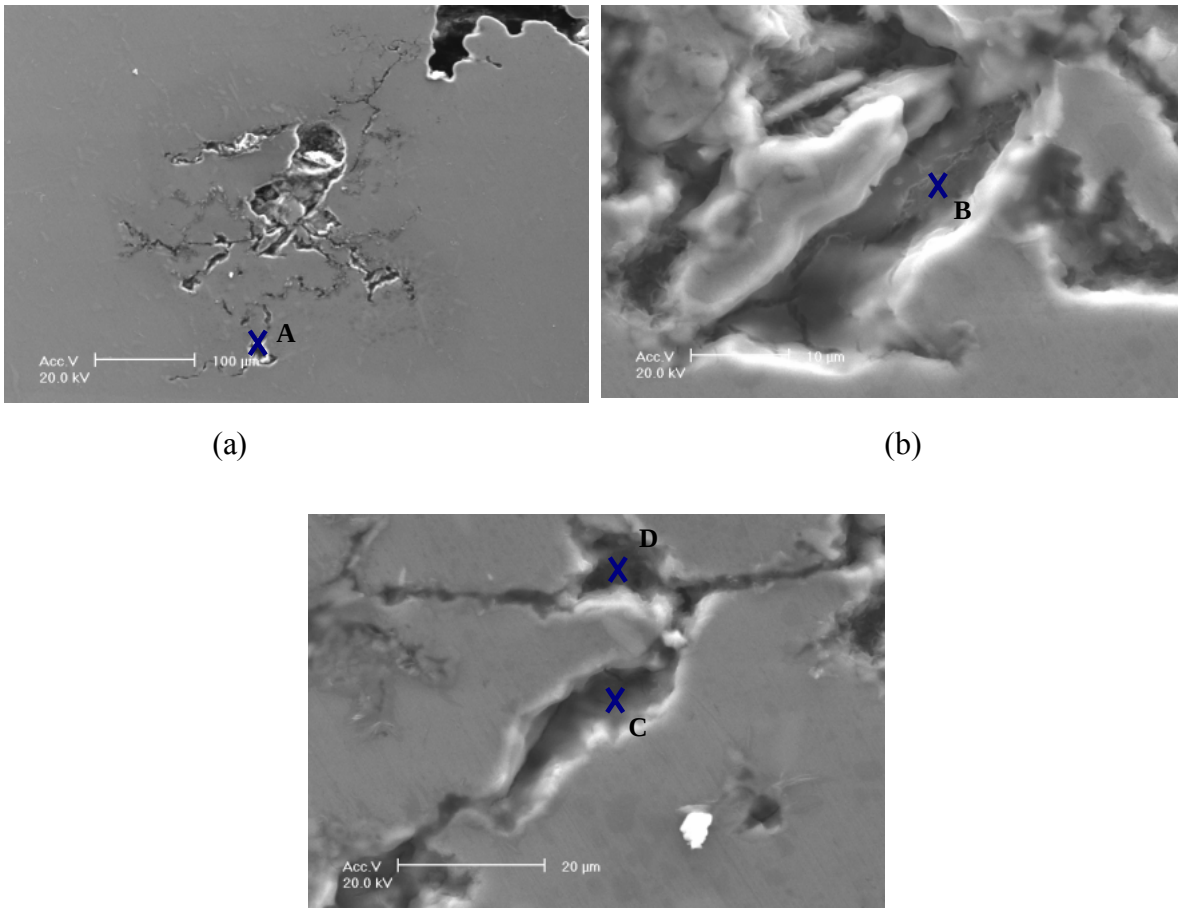

(a) (b)

(c)

Figure 4.54 The scanning electron micrographs of cross section of test bar obtained from low Fe, high hydrogen and high oxide film combination showing (a) oxide film network in the casting (b) and (c) the close-up observation of figure 4.55a

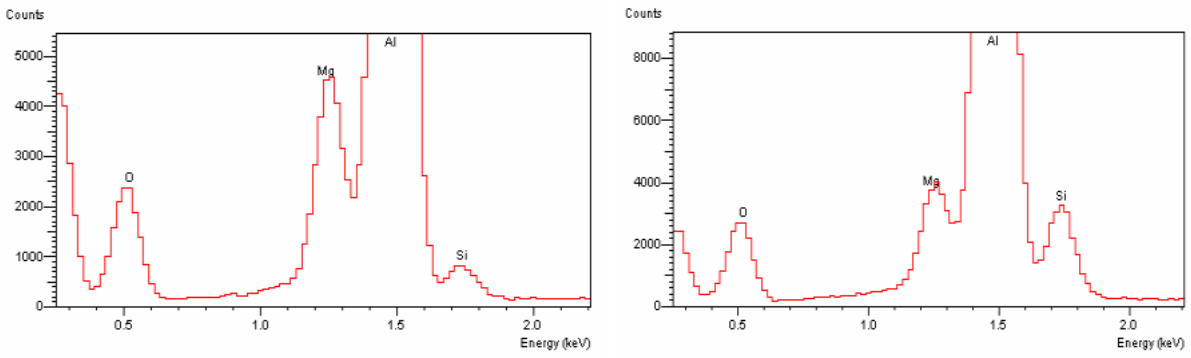

(a) (b)

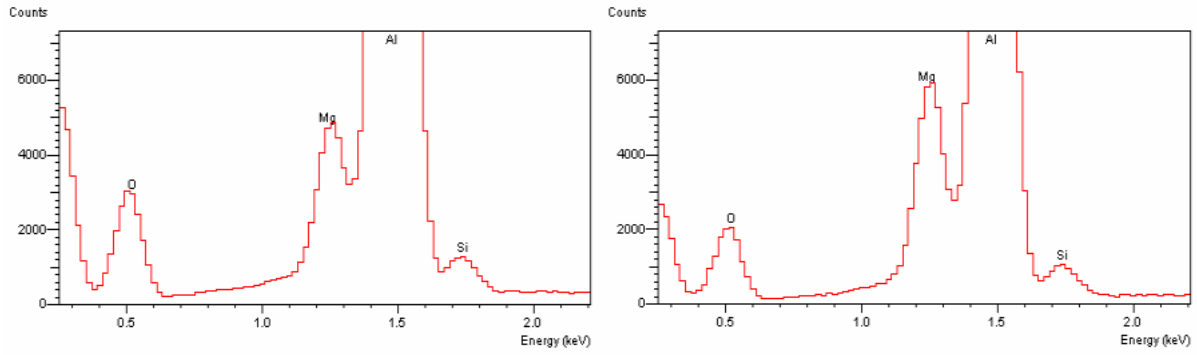

(c) (d)

Figure 4.55 The EDX analysis results obtained from points A to E in figure 4.54a to 4.54c.

An interaction between Fe-rich phases and porosity in the casting was also found in the SEM images. Figures 4.56a to 4.56b show back-scattered images of microstructures obtained from a heat-treated test bar of a high Fe, low hydrogen and high oxide film casting. Figure 4.57 shows an SEM image of porosity obtained from the high Fe, high hydrogen and low oxide film casting and Figure 4.58 shows associated EDX analysis. It can be clearly seen that Fe-rich phases were frequently found at the edge of pores in the castings. Furthermore, Figure 4.59 and the EDX analysis results in Figures 4.60a and 4.60b show that the internal surface of these pores also contained oxide films as did the pores in Figures 4.44 and 4.46. Similar evidence has been shown in Figures 4.61 and 4.62. These observations suggested interactions between Fe-rich phase, hydrogen porosity and oxide film, for example, that the β-Al_5FeSi phase that nucleated on the oxide film might influence the formation of porosity that also nucleated from the oxide film.

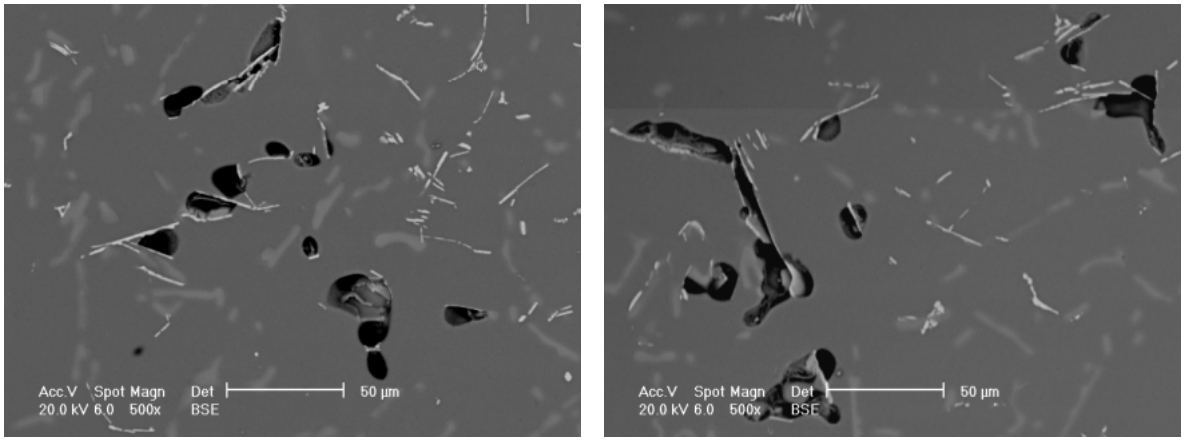

(a) (b)

Figure 4.56 The back-scattered electron images obtained from the high Fe, low hydrogen and high oxide film casting showing Fe-rich phase associated with porosity.

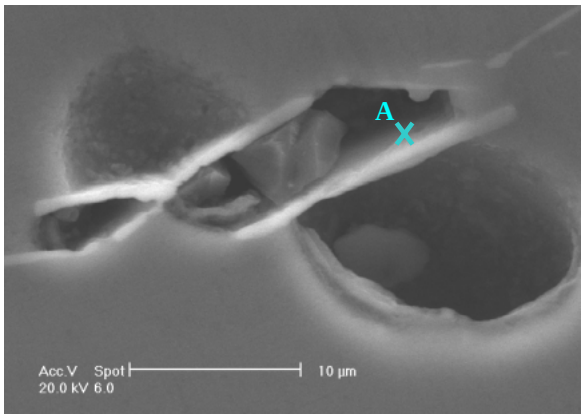

Figure 4.57 The scanning electron micrograph obtained from the high Fe, high hydrogen and low oxide film casting showing Fe-rich phase associated with the porosity

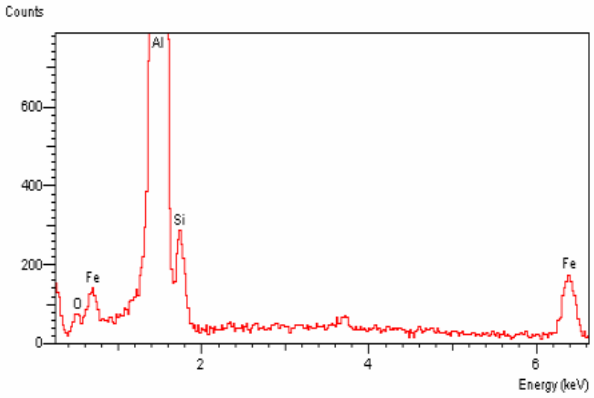

Figure 4.58 The EDX analysis result obtained from point A in figure 4.57.

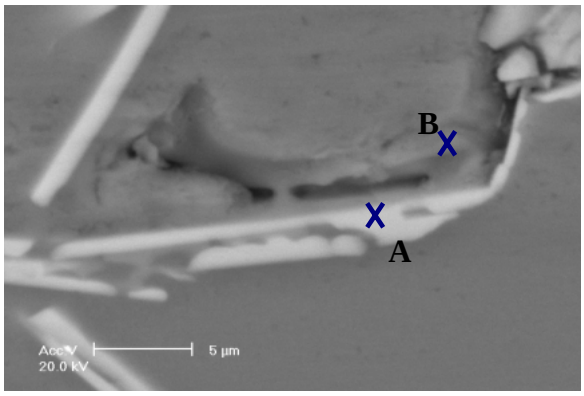

Figure 4.59 The scanning electron micrographs of cross section of runner obtained from high Fe, low hydrogen and high oxide film casting showing microporosity in the casting associated with Fe-rich phases.

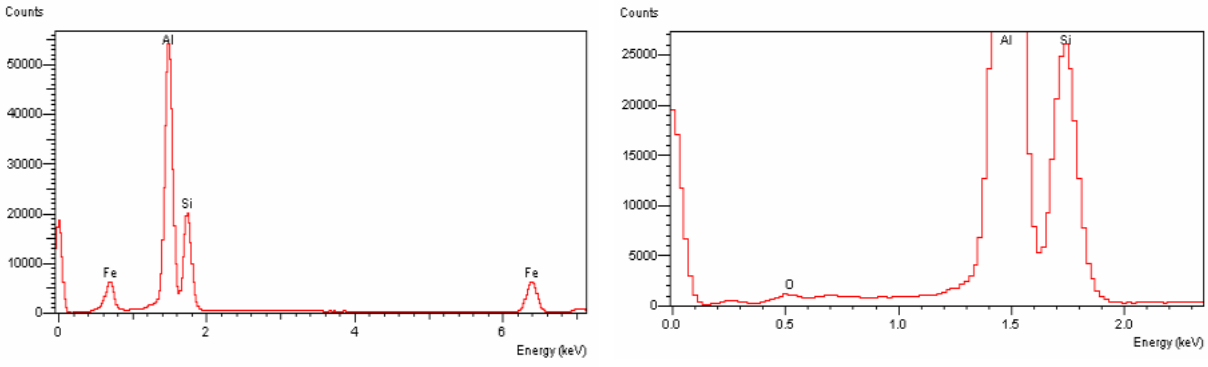

(a) (b)

Figure 4.60 The EDX analysis results obtained from points A and B in figure 4.59.

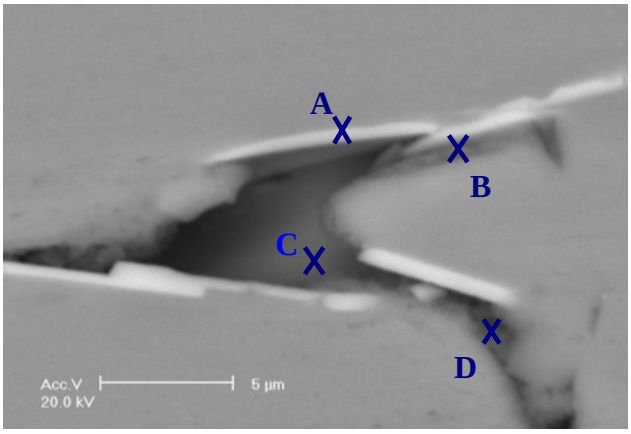

Figure 4.61 The scanning electron micrographs of cross section of runner obtained from high Fe, low hydrogen and high oxide film casting showing microporosity associated with the Fe-rich phases.

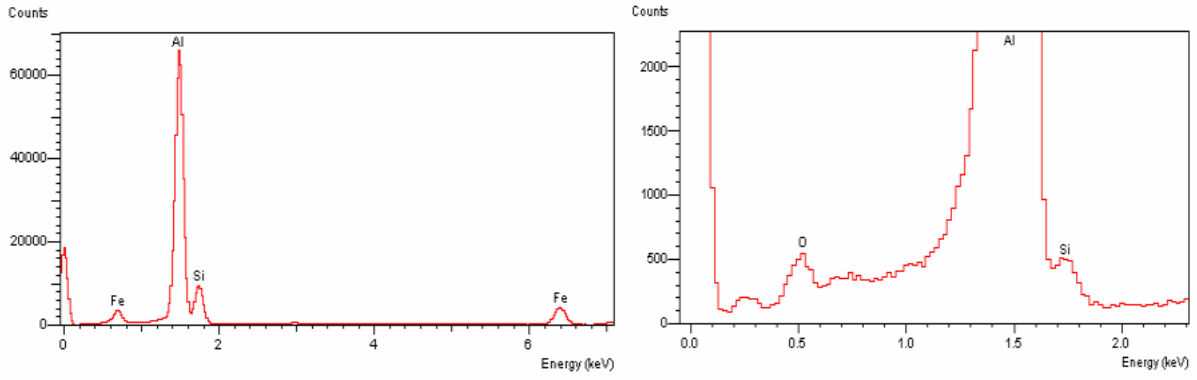

(a)

(b)

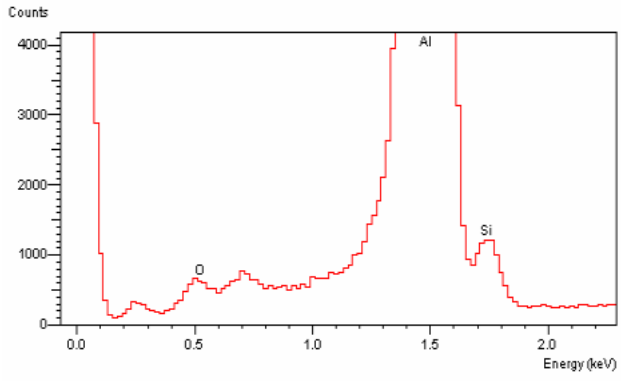

(c)

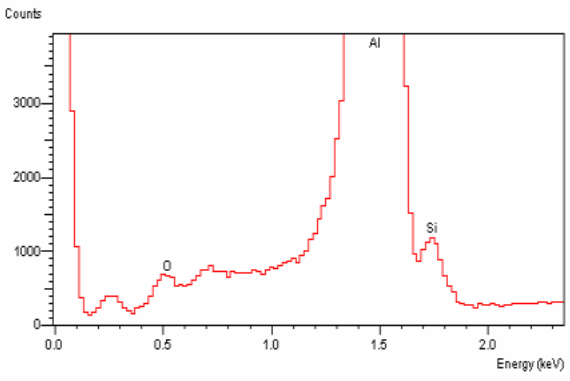

(d)

Figure 4.62 The EDX analysis results obtained from points A to D in figure 4.61.

4.1.6 Image analysis

A hundred images from each experimental combination were obtained from the runner bars, examined using an optical microscope and subjected to image analysis. Table 4.9 shows results of measured porosity area, number of pores per cm^2 and mean pore size obtained from the image analysis. As might be expected, increasing hydrogen content, from 0.1 to 0.45 ml/100g metal, resulted in an increase in the overall porosity area and mean pore size. For example, in the low Fe and high oxide film content castings the porosity area increased from 0.42 % to 3.66 % while the mean size of the pore increased from 283 to 2466 μm^2.

Table 4.9 Image analysis results obtained from 8 experimental combinations.

Combination	Pore area (%)	Number of pore per cm^2	Mean pore size (μm^2)
low Fe, low H_2, low oxide film	0.45	1424	314
low Fe, low H_2, high oxide film	0.42	1456	283
low Fe, high H_2, low oxide film	2.52	1113	2269
low Fe, high H_2, high oxide film	3.66	1488	2466
high Fe, low H_2, low oxide film	0.40	1747	227
high Fe, low H_2, high oxide film	0.48	2339	205
high Fe, high H_2, low oxide film	4.82	3683	1309
high Fe, high H_2, high oxide film	4.58	3583	1277

The increase in Fe content from 0.1 to 0.5 wt% resulted in a large increase in the number of pores. For example, in the low oxide film and high hydrogen gas castings, increasing the Fe content resulted in an increase in the number of pores from 1113 to 3683 pores per cm^2, (a three-fold increase). The Fe content also resulted in a noticeable change in area of porosity from 2.52 to 4.82%; while the size of the pore appeared to be reduced from 2269 to 1309 μm^2 when the Fe content increased.

The presence of oxide film slightly influenced the area of porosity and pore size since increasing oxide film content resulted in an increase in the pore area and pore size in

only the low Fe and high hydrogen content whereas there was no effect of oxide films in the other defect combinations. However, the oxide films introduced in this experiment had effects on the number of pores in the castings, for example, in the low Fe and low hydrogen castings, the number of pores increased by about 34% when the oxide film contents was increased.

Tables 4.10, 4.11 and 4.12 show the Yate's algorithm calculation for the area of porosity, number of pores and mean pore size results obtained from the image analysis data, respectively. Pareto diagrams illustrating the relative effects of Fe-rich phase, hydrogen gas, oxide films, and their interactions, on the porosity area, number of pores and size of pore are shown in Figures 4.63a, 4.63b and 4.63c respectively. The diagrams show that, as expected, hydrogen gas (column B) produced the greatest effect on porosity in this experiment, (with effects of about 3.5 % on the porosity area and about 1600 μm^2 on the size of pore). Increasing hydrogen content from 0.1 to 0.45 ml/100 g metal also resulted in an increase in the number of pores of about 725 pores per cm^2.

Increasing Fe-rich phase (column A) appeared to have the greatest effect on the number of pores (increasing them by about 1470 pore per cm^2) and also produced effects on the porosity area and size of pore (increasing area by about 0.8 % and decreasing pore size by about 580 μm^2). The Fe-rich phase, therefore, played an important role in the presence of porosity, particularly microporosity (i.e. < 100 μm diameter). Oxide films surprisingly had a negligible effect at the level introduced in this experiment. Effects of oxide films on porosity area, number of pores and size of pores were only about 0.2 %, 225 pores per cm^2 and 30 μm^2 respectively.

The Pareto diagrams also showed that an interaction between the Fe-rich phase and hydrogen content (column AB) had an effect on by increasing the porosity area of about 0.8 %, the number of pores of about 865 pores per cm^2 and on the pore size of about 500 μm^2. No significant effect associated with an interaction between Fe-rich phase and oxide films (column AC), an interaction between hydrogen gas and oxide film (column BC), and an interaction between Fe-rich phase, hydrogen gas and oxide film (column ABC), was observed.

Table 4.10 The effect of Fe-rich phase, hydrogen, oxide film and their interactions on the porosity area using Yate's algorithm.

	total	1	2	3	estimate of effect
(1)	0.45	0.85	8.19	17.33	4.33
A (effect of Fe-rich phase)	0.40	7.34	9.14	3.23	0.81
B (effect of hydrogen)	2.52	0.90	2.25	13.83	3.46
AB	4.82	8.24	0.98	3.21	0.80
C (effect of oxide film)	0.42	-0.05	6.49	0.95	0.24
AC	0.48	2.30	7.34	-1.27	-0.32
BC	3.66	0.06	2.35	0.85	0.21
ABC	4.58	0.92	0.86	-1.49	-0.37

Table 4.11 The effect of Fe-rich phase, hydrogen, oxide film and their interactions on the number of pores per cm^2 using Yate's algorithm.

	total	1	2	3	estimate of effect
(1)	1424	3171	7967	16833	4208
A (effect of Fe-rich phase)	1747	4796	8866	5871	1468
B (effect of hydrogen)	1113	3795	2893	2901	725
AB	3683	5071	2978	3459	865
C (effect of oxide film)	1456	323	1625	899	225
AC	2339	2570	1276	85	21
BC	1488	883	2247	-349	-87
ABC	3583	2095	1212	-1035	-259

Table 4.12 The effect of Fe-rich phase, hydrogen, oxide film and their inter- actions on the size of pore using Yate's algorithm.

	total	1	2	3	estimate of effect
(1)	314	541	4119	8350	2088
A (effect of Fe-rich phase)	227	3578	4231	-2314	-579
B (effect of hydrogen)	2269	488	-1047	6292	1573
AB	1309	3743	-1267	-1984	-496
C (effect of oxide film)	283	-87	3037	112	28
AC	205	-960	3255	-220	-55
BC	2466	-78	-873	218	55
ABC	1277	-1189	-1111	-238	-60

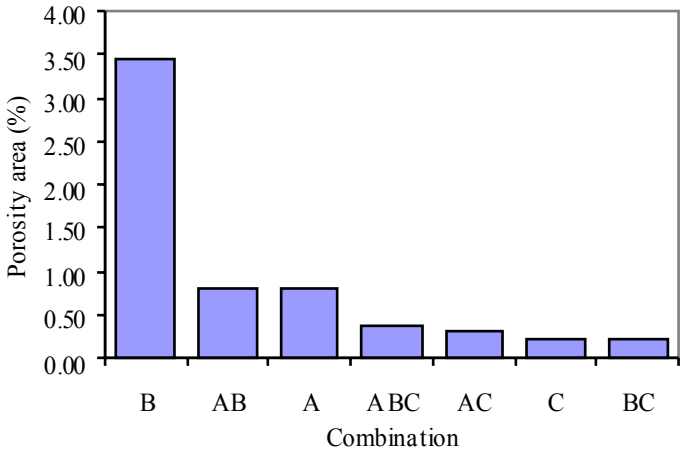

(a)

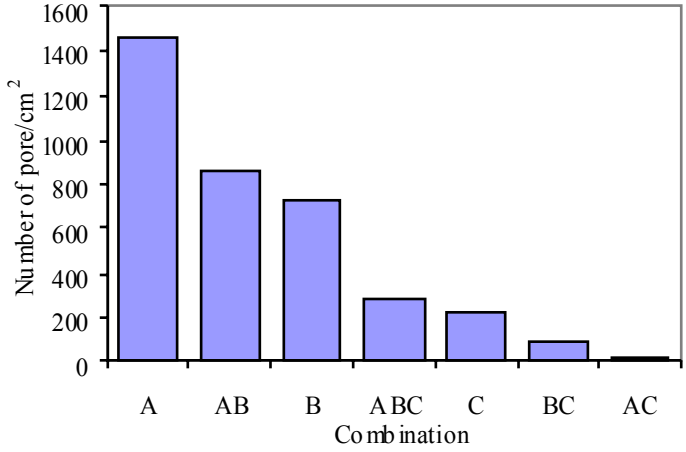

(b)

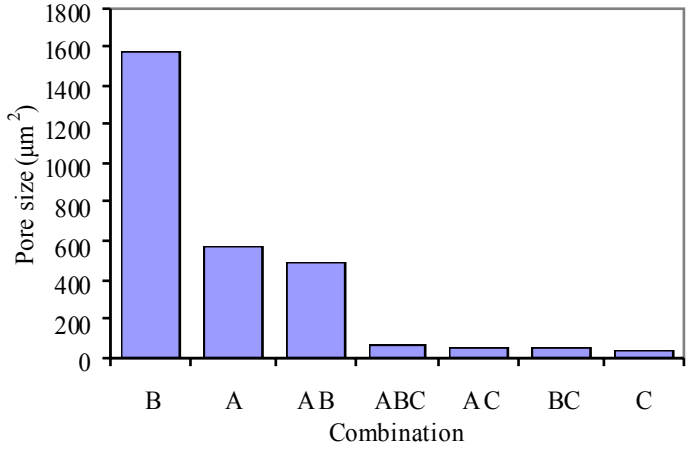

(c)

Figure 4.63 Pareto diagrams showing the effects of microstructural defects and their interrelationships on a) the porosity area, b) the number of pores per cm^2, and c) the pore size (A =Fe-rich phase, B = hydrogen, C = oxide films).